UNIVERSITY OF OSLO
Department of Geosciences
MetOs section

Mass transport induced by internal Kelvin waves

Master thesis in Geosciences Meteorology and oceanography

Eivind Støylen

22nd May 2008

Abstract

A two-layer system with a deep lower layer in a semi-infinite ocean is investigated theoretically. Tidal forcing is applied, and expressions for an internal Kelvin wave are derived. Terms of second order in wave amplitude are retained, to get the wave averaged drift in the flow. The along-shore wave is damped due to friction. Accordingly, the damping in wave drift is compensated by a second order mean motion normal to the direction of wave propagation. Furthermore, the second order momentum equations are shown to relate to the divergence of wave energy flux, in the same manner as barotropic waves.

The derived internal Kelvin wave theory is applied to a semi-enclosed basin. This basin has a constriction at the basin entrance in order to enhance internal wave generation. On the northern hemisphere, the wave propagates anti-clockwise around the basin. A numerical model is applied to examine this wave motion. It is shown that the waves obtained may induce a net circulation in the basin.

An attempt is made to connect the results from the semi-enclosed basin to the Van Mijen fjord in Svalbard. This fjord is ice-covered a large part of the year, preventing energy input from wind and enhancing internal wave motion. Numerical model results demonstrate an internal wave as predicted. However, the model assumptions do not fully resolve the complexity of the system. Further investigation is needed to understand the motion in this particular fjord.

Preface

Writing a master thesis is an interesting process. After the years at the university I like to believe that I have attained some level of knowledge. However, this year's work has taught me that although knowledge is important, you do not get any further without the ability to think for yourselves. This is a cliché of course, but nevertheless the truth stands. There is no book where I can look for answers. It took me some time to grasp the implications of this fact.

As such, discussions with more experienced people has been an essential part of this work. I will first and formost thank my tutors professor Jan Erik Weber and postdoc Kai Håkon Christensen. Weber has provided solid guidance through the year, always with a way out of any problem occuring. Christensen has given second opinions, and been a great support through the frustrating phase of designing reasonable model runs. I want to thank Christensen specially for giving me the opportunity to travel to Gøteborg and speek about our work at the university there.

I want to direct a thank to professor Bjørn Gjevik for the numerical model he provided. The discussions we had were interesting, and I hope we get an opportunity to work more on this model at a later time. Also I want to mention professor Anders Stigebrandt from the University in Gøteborg, for useful input regarding flow patterns in the Van Mijen fjord. Finally I want to thank everyone at the metos department. No matter where I direct my questions, people are always willing to help out. Thank you all for providing an inspiring work environment for me.

Contents

List of Figures

Chapter 1

Introduction

Wave motion in fluids is associated with motion of material fluid particles. When looking at uni-directional waves propagating on a surface, the most convenient way is usually to approximate the particle motion as oscillatory motion with closed trajectories. To the leading order this is a fairly solid approximation for many wave types. However, when studying the problem more closely, we realize that the paths are not always closed. When averaging over a wave period, there is often a net displacement of the particle in the direction of wave propagation. In fact, the wave motion can induce a small current in the direction of wave propagation. This *wave drift* is proportional to the square of the wave amplitude, first pointed out by Stokes (1847). His theory has formed the basis of a broad research area, as the phenomenon is applicable to all kinds of waves.

In the ocean, waves occur both at the ocean surface as well as within the fluid. If there is a pronounced vertical density gradient present, e.g. a *pycnocline*, there may be waves propagating here. These waves have potentially much larger amplitudes than surface waves, due to the relative density differences reducing the effects of gravity here. In such a system, the wave drift is accordingly larger at the pycnocline than at the surface.

In this thesis we study the wave drift in internal Kelvin waves. Kelvin waves are trapped waves propagating along a boundary, often the coast as a result of influence from the Coriolis force. Internal Kelvin waves are similar to surface Kelvin waves, however these propagate along the pycnocline in a stratified fluid. Many fjords are stratified in a way that support such wave motion. The wave will then propagate around the fjord, in some cases damped by friction. The corresponding wave drift induces an along-shore current. We aim at studying how this current eventually may set up a circulation pattern in the fjord.

The structure of the thesis is as follows: In chapter 2 we derive the basic equations for a two-layer system. In chapter 3 we linearize and introduce a coast, to derive expressions for an internal Kelvin wave in a semi-infinite ocean. In chapter 4, the nonlinear properties of this motion is discussed. In chapter 5 we introduce a theoretical basin with a narrow opening. A numerical model is applied to illustrate the wave motion for this geometry. Furthermore, the drift properties and an possible circulation pattern are discussed. In chapter 6 we look at the Van Mijen fjord in Svalbard. This fjord is ice-covered much of the year, preventing energy input from wind. We apply our results here and discuss the possibilities of a wave-induced circulation pattern in this fjord.

Chapter 2

Two-layer model

The density of the water in a typical fjord is slowly increasing from the surface to a certain depth where a jump in the density appears. This jump is the pycnocline, beneath which the density slowly approaches some maximum value. This density structure is found in many fjords, and is a concequence of freshwater runoff from rivers or glaciers. The freshwater is lighter than the surrounding saltier water, and accordingly the saltier water is situated beneath the freshwater after stability is obtained.

When describing motion in such a system, it is often convenient to approximate the density distribution as a two layer system. A typical pycnocline depth is defined, and then the density is set constant above and below this break point. Such an approach will be used in this thesis. In this chapter we derive equations governing the motion in each layer.

2.1 Basic equations

Consider a two-layer system as illustrated in figure 2.1. The orthogonal coordinate system x, y, z has unit vectors $\mathbf{i}, \mathbf{j}, \mathbf{k}$. The corresponding current components are u_i, v_i, w_i, where $i = 1, 2$ is the upper and lower layer respectively. The mean upper layer thickness is H_1, and the surface coordinate is $z = \eta(x, y, t)$. The bottom at $z = -H_2(x, y)$ is assumed stationary, and the interface coordinate is $z = \xi(x, y, t)$. At the surface, we allow a pressure $p = P_s(x, y, t)$, which is variable both in time and space. The upper and lower layer densities are ρ_1 and ρ_2 respectively. These are constant, and to maintain stability we assume $\rho_2 > \rho_1$.

The equation of motion

The equation of motion in each layer on a rotating earth may be written

$$\frac{D\mathbf{u}_i}{dt} = -2\boldsymbol{\Omega} \times \mathbf{u}_i + \mathbf{g} - \frac{1}{\rho_i}\nabla p_i - \mathbf{F}_i. \tag{2.1.1}$$

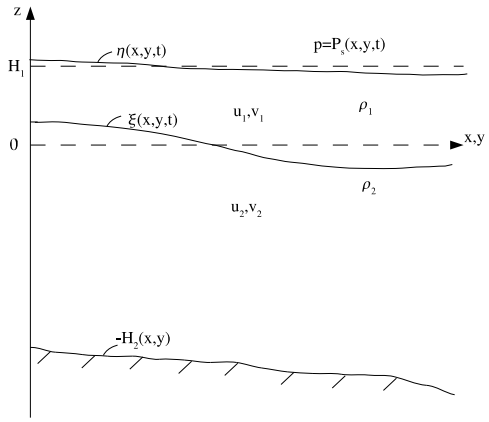

Figure 2.1: *The two-layer model, z is vertical axis. Mean layer thickness is H_i, density ρ_i and horizontal current components u_i, v_i. i=1,2 is upper and lower layer respectively. η and ξ are surface and interface heights respectively.*

Here, $\mathbf{F}_i$ is a force summing up all dissipative forces removing energy from the system. If we are far from the equator we may neglect the vertical component of the Coriolis force, i.e. $\mathbf{\Omega} \times \mathbf{k} = 0$. The Coriolis parameter f is defined as

$$f = 2\,\Omega \sin\phi, \tag{2.1.2}$$

where ϕ is latitude and Ω is the angular frequency of the earth. The Coriolis term may accordingly be approximated as:

$$-2\,\mathbf{\Omega} \times \mathbf{u}_i \approx -2\,\Omega \sin\phi\,\mathbf{k} \times \mathbf{u}_i = f v_i\,\mathbf{i} - f u_i\,\mathbf{j}. \tag{2.1.3}$$

The pressure is assumed hydrostatic, so the following holds:

$$\frac{\partial p_i}{\partial z} = -\rho_i\, g. \tag{2.1.4}$$

The pressure must be continous at the interface, so $p_1 = p_2$ at $z = \xi$. Integrating (2.1.4) from the surface to some height z, the expression for the pressure is given:

$$\left.\begin{aligned} p_1 &= -\rho_1 g z + \rho_1 g(H_1 + \eta) + P_s \\ p_2 &= -\rho_2 g z + g(\rho_2 - \rho_1)\xi + \rho_1 g(H_1 + \eta) + P_s. \end{aligned}\right\} \tag{2.1.5}$$

We want to integrate equation (2.1.1) in the vertical between material surfaces. Accordingly, we define the vertically integrated fluxes as follows:

$$\left.\begin{aligned} \int_{\xi}^{H_1+\eta} u_1 dz \equiv U_1, \quad \int_{\xi}^{H_1+\eta} v_1 dz \equiv V_1 \\ \int_{-H_2}^{\xi} u_2 dz \equiv U_2, \quad \int_{-H_2}^{\xi} v_2 dz \equiv V_2. \end{aligned}\right\} \tag{2.1.6}$$

The integrated term $\mathbf{F}_i$ is separated in various stress terms, i.e.

$$\left.\begin{aligned}\int_{\xi}^{H_1+\eta} \mathbf{F}_1\, dz &= \left(\frac{\tau_s^{(x)}}{\rho_1} - \frac{\tau_i^{(x)}}{\rho_1}\right)\mathbf{i} + \left(\frac{\tau_s^{(y)}}{\rho_1} - \frac{\tau_i^{(y)}}{\rho_1}\right)\mathbf{j} \\ \int_{-H_2}^{\xi} \mathbf{F}_2\, dz &= \left(\frac{\tau_i^{(x)}}{\rho_2} - \frac{\tau_b^{(x)}}{\rho_2}\right)\mathbf{i} + \left(\frac{\tau_i^{(y)}}{\rho_2} - \frac{\tau_b^{(y)}}{\rho_2}\right)\mathbf{j}.\end{aligned}\right\} \tag{2.1.7}$$

Here, τ_s is surface stress on the upper layer, τ_i is internal stress between the layers, and τ_b is bottom stress on the lower layer. Superscripts indicate that the stress may not be the same in the x and y direction.

Let us look at the horizontal components of equation (2.1.1). We separate in two layers and integrate in the vertical, inserting (2.1.3), (2.1.5), (2.1.6) and (2.1.7). We then arrive at the following set of equations governing the motion:

$$\frac{DU_1}{dt} - fV_1 = -gh_1\frac{\partial \eta}{\partial x} - \frac{h_1}{\rho_1}\frac{\partial P_s}{\partial x} + \frac{\tau_s^{(x)}}{\rho_1} - \frac{\tau_i^{(x)}}{\rho_1} \tag{2.1.8}$$

$$\frac{DV_1}{dt} + fU_1 = -gh_1\frac{\partial \eta}{\partial y} - \frac{h_1}{\rho_1}\frac{\partial P_s}{\partial y} + \frac{\tau_s^{(y)}}{\rho_1} - \frac{\tau_i^{(y)}}{\rho_1} \tag{2.1.9}$$

$$\frac{DU_2}{dt} - fV_2 = -\frac{\rho_1}{\rho_2}gh_2\frac{\partial \eta}{\partial x} - g_*h_2\frac{\partial \xi}{\partial x} - \frac{h_2}{\rho_2}\frac{\partial P_s}{\partial x} + \frac{\tau_i^{(x)}}{\rho_2} - \frac{\tau_b^{(x)}}{\rho_2} \tag{2.1.10}$$

$$\frac{DV_2}{dt} + fU_2 = -\frac{\rho_1}{\rho_2}gh_2\frac{\partial \eta}{\partial y} - g_*h_2\frac{\partial \xi}{\partial y} - \frac{h_2}{\rho_2}\frac{\partial P_s}{\partial y} + \frac{\tau_i^{(y)}}{\rho_2} - \frac{\tau_b^{(y)}}{\rho_2}. \tag{2.1.11}$$

Here

$$h_1 = H_1 + \eta - \xi \tag{2.1.12}$$

$$h_2 = H_2 + \xi \tag{2.1.13}$$

$$g_* = g\frac{\rho_2 - \rho_1}{\rho_2} \tag{2.1.14}$$

are the total layer depths in upper and lower layer, and the reduced gravity term, respectively.

The continuity equation

The continuity equation in a fluid with constant density is

$$\nabla \cdot \mathbf{u} = 0. \tag{2.1.15}$$

In order to integrate this equation in the vertical, we need the following kinematic boundary conditions on w, following the formulation of LeBlond

and Mysak (1989):

$$\left.\begin{aligned} w_1 &= \frac{\partial \eta}{\partial t} + u_1\frac{\partial \eta}{\partial x} + v_1\frac{\partial \eta}{\partial y}, && z = H_1 + \eta \\ w_2 = w_1 &= \frac{\partial \xi}{\partial t} + u_1\frac{\partial \xi}{\partial x} + v_1\frac{\partial \xi}{\partial y}, && z = \xi \\ w_2 &= -u_2\frac{\partial H_2}{\partial x} - v_2\frac{\partial H_2}{\partial y} \approx 0, && z = -H_2. \end{aligned}\right\} \tag{2.1.16}$$

It is here assumed that H_2 is sufficiently large for $\mathbf{u}_2$ to be negligibly small, close to the bottom (if the bottom is flat, conditions (2.1.16) are exact). Now, using Leibniz' rule of differentiation of integrals, we get the exact relation:

$$\frac{\partial U_1}{\partial x} + \frac{\partial V_1}{\partial y} = -\frac{\partial \eta}{\partial t} + \frac{\partial \xi}{\partial t} \tag{2.1.17}$$

$$\frac{\partial U_2}{\partial x} + \frac{\partial V_2}{\partial y} = -\frac{\partial \xi}{\partial t}. \tag{2.1.18}$$

2.2 Method of solutions, upper layer equations

In this section we want to derive simplified equations regarding the motion in the upper layer. The equations derived in the previous section are general, valid for any choice of layer thickness and surface amplitude. We will in the following restrict ourselves to motion where surface amplitudes are small compared to the interface amplitudes, and with a very deep lower layer. We will also rewrite the material derivative so the convective terms appear explicitly.

With equation (2.1.15), the material derivative may be written

$$\frac{Du_1}{dt} = \frac{\partial u_1}{\partial t} + \mathbf{u_1}\cdot\nabla u_1 = \frac{\partial u_1}{\partial t} + \nabla\cdot(\mathbf{u_1}u_1), \tag{2.2.1}$$

using the rule of differentiation of products. Integrating through the upper layer and using Leibniz' rule for integration of integrals we get the following for the material acceleration of the fluid column:

$$\begin{aligned} \int_\xi^{H_1+\eta}\frac{Du_1}{dt}dz = {} & \frac{\partial}{\partial t}\int_\xi^{H_1+\eta} u_1 dz - \frac{\partial \eta}{\partial t}u_1|_{z=(H_1+\eta)} + \frac{\partial \xi}{\partial t}u_1|_{z=\xi} \\ & + \frac{\partial}{\partial x}\int_\xi^{H_1+\eta} u_1u_1 dz - \frac{\partial \eta}{\partial x}u_1u_1|_{z=(H_1+\eta)} + \frac{\partial \xi}{\partial x}u_1u_1|_{z=\xi} \\ & + \frac{\partial}{\partial y}\int_\xi^{H_1+\eta} v_1u_1 dz - \frac{\partial \eta}{\partial y}v_1u_1|_{z=(H_1+\eta)} + \frac{\partial \xi}{\partial y}v_1u_1|_{z=\xi} \\ & + w_1u_1|_{z=(H_1+\eta)} - w_1u_1|_{z=\xi} \end{aligned} \tag{2.2.2}$$

Rearranging (2.2.2) and using (2.1.16), many terms disappear. The result is valid in both layers and is as follows, where the flux terms are defined in (2.1.6):

$$\left.\begin{aligned}
\int_{\xi}^{H_1+\eta} \frac{Du_1}{dt} dz &= \frac{\partial U_1}{\partial t} + \frac{\partial}{\partial x}\int_{\xi}^{H_1+\eta} u_1 u_1 dz + \frac{\partial}{\partial y}\int_{\xi}^{H_1+\eta} u_1 v_1 dz \\
\int_{\xi}^{H_1+\eta} \frac{Dv_1}{dt} dz &= \frac{\partial V_1}{\partial t} + \frac{\partial}{\partial x}\int_{\xi}^{H_1+\eta} u_1 v_1 dz + \frac{\partial}{\partial y}\int_{\xi}^{H_1+\eta} v_1 v_1 dz \\
\int_{-H_2}^{\xi} \frac{Du_2}{dt} dz &= \frac{\partial U_2}{\partial t} + \frac{\partial}{\partial x}\int_{-H_2}^{\xi} u_2 u_2 dz + \frac{\partial}{\partial y}\int_{-H_2}^{\xi} u_2 v_2 dz \\
\int_{-H_2}^{\xi} \frac{Dv_2}{dt} dz &= \frac{\partial V_2}{\partial t} + \frac{\partial}{\partial x}\int_{-H_2}^{\xi} u_2 v_2 dz + \frac{\partial}{\partial y}\int_{-H_2}^{\xi} v_2 v_2 dz.
\end{aligned}\right\} \tag{2.2.3}$$

Before inserting these expressions back in the equations of motion, we need to perform an order of magnitude approach on the integration limits to simplify further. One of the integral terms in (2.2.3) may be approximated as:

$$\begin{aligned}
\int_{\xi}^{H_1+\eta} u_1^2 dz &\approx \int_0^{H_1} u_1^2 dz - \xi\, u_1|^2_{(z=0)} + \eta\, u_1|^2_{(z=H_1)} \\
&\approx \int_0^{H_1} u_1^2 dz.
\end{aligned} \tag{2.2.4}$$

Here it is assumed that H_1 is much larger than ξ and η. This argument is valid for the other integration terms in (2.2.3). We may thus insert these expressions back in equations (2.1.8)-(2.1.11):

$$\begin{aligned}
\frac{\partial U_1}{\partial t} - fV_1 =& -gh_1\frac{\partial \eta}{\partial x} - \frac{h_1}{\rho_1}\frac{\partial P_s}{\partial x} + \frac{\tau_s^{(x)}}{\rho_1} - \frac{\tau_i^{(x)}}{\rho_1} \\
&- \frac{\partial}{\partial x}\int_0^{H_1} u_1 u_1 dz - \frac{\partial}{\partial y}\int_0^{H_1} u_1 v_1 dz
\end{aligned} \tag{2.2.5}$$

$$\begin{aligned}
\frac{\partial V_1}{\partial t} + fU_1 =& -gh_1\frac{\partial \eta}{\partial y} - \frac{h_1}{\rho_1}\frac{\partial P_s}{\partial y} + \frac{\tau_s^{(y)}}{\rho_1} - \frac{\tau_i^{(y)}}{\rho_1} \\
&- \frac{\partial}{\partial x}\int_0^{H_1} u_1 v_1 dz - \frac{\partial}{\partial y}\int_0^{H_1} v_1 v_1 dz
\end{aligned} \tag{2.2.6}$$

$$\begin{aligned}
\frac{\partial U_2}{\partial t} - fV_2 =& -\frac{\rho_1}{\rho_2}gh_2\frac{\partial \eta}{\partial x} - g_* h_2\frac{\partial \xi}{\partial x} - \frac{h_2}{\rho_2}\frac{\partial P_s}{\partial x} + \frac{\tau_i^{(x)}}{\rho_2} - \frac{\tau_b^{(x)}}{\rho_2} \\
&- \frac{\partial}{\partial x}\int_{-H_2}^{0} u_2 u_2 dz - \frac{\partial}{\partial y}\int_{-H_2}^{0} u_2 v_2 dz
\end{aligned} \tag{2.2.7}$$

$$\begin{aligned}
\frac{\partial V_2}{\partial t} + fU_2 =& -\frac{\rho_1}{\rho_2}gh_2\frac{\partial \eta}{\partial y} - g_* h_2\frac{\partial \xi}{\partial y} - \frac{h_2}{\rho_2}\frac{\partial P_s}{\partial y} + \frac{\tau_i^{(y)}}{\rho_2} - \frac{\tau_b^{(y)}}{\rho_2} \\
&- \frac{\partial}{\partial x}\int_{-H_2}^{0} u_2 v_2 dz - \frac{\partial}{\partial y}\int_{-H_2}^{0} v_2 v_2 dz
\end{aligned} \tag{2.2.8}$$

We assume a deep lower layer. Dividing the lower layer momentum equations through by h_2 and letting $h_2 \to \infty$, the following balance appears:

$$g\frac{\partial \eta}{\partial x} = -\frac{\rho_2}{\rho_1} g_* \frac{\partial \xi}{\partial x} - \frac{1}{\rho_1}\frac{\partial P_s}{\partial x} \tag{2.2.9}$$

$$g\frac{\partial \eta}{\partial y} = -\frac{\rho_2}{\rho_1} g_* \frac{\partial \xi}{\partial y} - \frac{1}{\rho_1}\frac{\partial P_s}{\partial y}. \tag{2.2.10}$$

This is a relation between pressure forces, namely the gradient in surface height on the left side, and the gradient in interface height and a surface pressure gradient on the right side. (2.2.9) and (2.2.10) are inserted to the upper moment equations to eliminate the surface pressure term.

We now assume that the interface height $|\xi|$ is much larger than the surface height $|\eta|$. Then we may approximate $h_1 \approx H_1 - \xi$. Using this approximation we may also simplify the continuity equation (2.1.17). Finally, we write down the resulting upper layer equations for baroclinic two-layer motion:

$$\begin{aligned}\frac{\partial U_1}{\partial t} - fV_1 - c_1^2\frac{\partial \xi}{\partial x} =& \frac{\tau_s^{(x)}}{\rho_1} - \frac{\tau_i^{(x)}}{\rho_1} - \frac{g_*}{2}\frac{\partial(\xi^2)}{\partial x} \\ &- \frac{\partial}{\partial x}\int_0^{H_1} u_1 u_1 dz - \frac{\partial}{\partial y}\int_0^{H_1} u_1 v_1 dz \end{aligned} \tag{2.2.11}$$

$$\begin{aligned}\frac{\partial V_1}{\partial t} + fU_1 - c_1^2\frac{\partial \xi}{\partial y} =& \frac{\tau_s^{(y)}}{\rho_1} - \frac{\tau_i^{(y)}}{\rho_1} - \frac{g_*}{2}\frac{\partial(\xi^2)}{\partial y} \\ &- \frac{\partial}{\partial x}\int_0^{H_1} u_1 v_1 dz - \frac{\partial}{\partial y}\int_0^{H_1} v_1 v_1 dz \end{aligned} \tag{2.2.12}$$

$$\frac{\partial \xi}{\partial t} = \frac{\partial U_1}{\partial x} + \frac{\partial V_1}{\partial y}. \tag{2.2.13}$$

Here, $c_1 = \sqrt{g_* H_1}$ is the internal phase speed. Since we integrate between material surfaces in the vertical, information on the wave drift is maintained in this equation set (see Appendix A).

In the next chapters we will attempt to solve the equations (2.2.11)-(2.2.13), using an order of magnitude approach. Assuming wave motion, we formally introduce an ordering parameter $\epsilon = |\hat{\xi}k| \ll 1$, which is the wave steepness. The variables may then be written:

$$\left.\begin{aligned} U_1 &= \epsilon U^{(1)} + \epsilon^2 U^{(2)} + ... \equiv \tilde{U} + \bar{U} + \mathcal{O}|\epsilon^3| \\ V_1 &= \epsilon V^{(1)} + \epsilon^2 V^{(2)} + ... \equiv \tilde{V} + \bar{V} + \mathcal{O}|\epsilon^3| \\ \xi &= \epsilon \xi^{(1)} + \epsilon^2 \xi^{(2)} + ... \equiv \tilde{\xi} + \bar{\xi} + \mathcal{O}|\epsilon^3|. \end{aligned}\right\} \tag{2.2.14}$$

The motion is here separated in two parts, where the $\tilde{(\cdot)}$ and the $\bar{(\cdot)}$ are defined as first and second order motion respectively.

Chapter 3

Linear theory

Towards the end of the previous chapter, a method of expanding our variables is introduced. In this chapter we will utilize the expansion (2.2.14) to look at the equation set (2.2.11)-(2.2.13) keeping only terms to $\mathcal{O}(\epsilon)$. We will simplify and assume a linear friction, giving us a strictly linear equation set. The geometry of the problem is defined as a semi-infinite ocean with a coast. An oscillating driving force of constant frequency is applied. Expressions for the first order solution are then derived, showing the dominant motion in this geometry. Henceforth we neglect subscripts on U and V; the motion of interest is the upper layer motion.

3.1 Modelling the friction

The stress terms in equations (2.2.11) and (2.2.12) may be parametrized in various ways. We will for simplicity choose a linear bulk/Rayleigh friction. The stress terms are assumed proportional to the mean upper layer flow, and we define a friction coefficient K as follows:

$$\frac{\tau_s^{(x)}}{\rho_1} - \frac{\tau_i^{(x)}}{\rho_1} \equiv -KU, \qquad \frac{\tau_s^{(y)}}{\rho_1} - \frac{\tau_i^{(y)}}{\rho_1} \equiv -KV. \tag{3.1.1}$$

The dimension of K is time^{-1}.

3.2 Results for a straight coast

We will now simplify our equations, and derive the first order motion for a semi-infinite coast. The geometry is illustrated in figure 3.1. There is a straight impermeable coast at $y = 0$, and the ocean stretches to infinity in positive x and y. At $x = 0$ we assume an internal wave with amplitude $\hat{\xi}$, constant frequency ω and wave number $\mathbf{k} = k\mathbf{i} + l\mathbf{j}$. As we will look at ocean motion far from the equator, let us concider forcing from the tidal

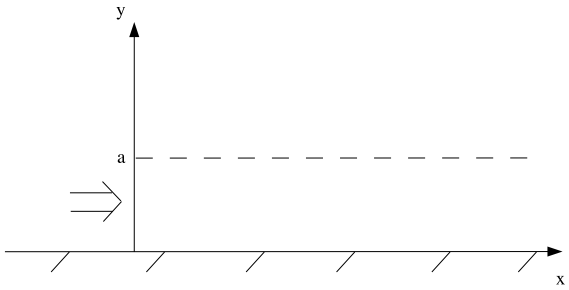

Figure 3.1: *Top-down illustration of the geometry with a straight coast at y=0. Arrow indicates internal wave entering from the left. The extent of the wave trapped region is indicated by the parameter a.*

M_2-component. The period of the motion is accordingly 12.42 hours. The motion is assumed regular for large x and y. We will now derive the equations of motion to the first order of ϵ, see (2.2.14). Inserting these expansions into equations (2.2.11)-(2.2.13) and neglecting terms of $\mathcal{O}(\epsilon)^2$, we get the following linear first order equations for the upper layer:

$$\frac{\partial \tilde{U}}{\partial t} - f\tilde{V} - {c_1}^2 \frac{\partial \tilde{\xi}}{\partial x} = -K\tilde{U} \tag{3.2.1}$$

$$\frac{\partial \tilde{V}}{\partial t} + f\tilde{U} - {c_1}^2 \frac{\partial \tilde{\xi}}{\partial y} = -K\tilde{V} \tag{3.2.2}$$

$$\frac{\partial \tilde{\xi}}{\partial t} = \frac{\partial \tilde{U}}{\partial x} + \frac{\partial \tilde{V}}{\partial y}. \tag{3.2.3}$$

The waves entering at $x = 0$ are assumed to be spatially damped with damping coefficient α. The scale of damping is assumed to be much larger than one wavelength, i.e. $|\alpha| \ll |k|$. The assumed motion is quasistationary, i.e. constant frequency and friction independent of time. The motion is trapped by rotation and should accordingly propagate along the coast and decay outward to $y = a$. We assume the following form of the wave, which should be applicable to our equation set:

$$\tilde{\xi} = \hat{\xi} e^{-(\alpha x + y/a)} e^{i(kx + ly - \omega t)} \tag{3.2.4}$$

All constants in this expression are real and positive, and $i = \sqrt{-1}$ is the complex unit. From equations (3.2.1)-(3.2.3) it is evident that $\tilde{U}$ and $\tilde{V}$ must be on the same form as $\tilde{\xi}$. Furthermore, using the boundary condition $\tilde{V}|_{y=0} = 0$ we realize that $\tilde{V}$ is zero everywhere. Now from equation (3.2.2) $\tilde{U}$ is readily found:

$$\tilde{U} = \frac{c_1^2}{f} \hat{\xi}\, e^{-(\alpha x + y/a)} e^{i(kx + ly - \omega t)} (-1/a + il) \tag{3.2.5}$$

With the form of the solution at hand, a derivation of the dispersion relation is needed to fully determine the solution. Inserting (3.2.5) in equations (3.2.1) and (3.2.3) reveals two complex equations to determine the four real constants k, α, l and a:

$$(l + i/a)(\omega + iK) = if(k + i\alpha) \tag{3.2.6}$$

$$\frac{i\omega f}{c_1^2} = (l + i/a)(k + i\alpha) \tag{3.2.7}$$

Eliminating $(l + i/a)$ gives the following relation:

$$k^2 - \alpha^2 = \omega^2/c_1^2 \tag{3.2.8}$$

$$2k\alpha = \omega K/c_1^2 \tag{3.2.9}$$

$$\Rightarrow k^2 = \frac{\omega^2}{2c_1^2}\left[1 \pm \sqrt{1 + \frac{K^2}{\omega^2}}\right] \tag{3.2.10}$$

We need an additional condition to simplify this relation further. As suggested we let $|k| >> |\alpha|$. From (3.2.8) it follows that $k^2 = \omega^2/{c_1}^2$ to the leading order. We recognize this as the equivalent to the dispersion relation of free surface waves without friction in shallow water. Let us then demand the following:

$$(K/\omega)^2 \ll 1, \tag{3.2.11}$$

which means that there is an upper limit to the choices of friction coefficient values applicable to our solution. Inserting (3.2.11) in (3.2.10), expanding and neglecting terms of $\mathcal{O}(K/\omega)^3$, we get:

$$k^2 \approx \frac{\omega^2}{c_1^2}\left[1 + \frac{1}{4}\frac{K^2}{\omega^2}\right] \Rightarrow k \approx \frac{\omega}{c_1}\left[1 + \frac{1}{8}\frac{K^2}{\omega^2}\right]. \tag{3.2.12}$$

Accordingly, if we neglect $(K/\omega)^2$ in (3.2.12), we are left with the same result as if we neglect α^2 in (3.2.8).

It is now a matter of simple algebra and similar series expansions to obtain the rest of the results, all summarized below and letting the real part of the solutions represent the physical values. Note that terms of $\mathcal{O}(K/\omega)^3$

are neglected:

$$\tilde{\xi} = \hat{\xi} e^{-\alpha x - y/a} \cos(kx + ly - \omega t) \tag{3.2.13}$$

$$\tilde{U} = -c_1 \hat{\xi} e^{-\alpha x - y/a} \cdot \left[\left(1 - \frac{3}{8} \frac{K^2}{\omega^2} \right) \cos(kx + ly - \omega t) + \right.$$
$$\left. + \frac{K}{2\omega} \sin(kx + ly - \omega t) \right] \tag{3.2.14}$$

$$\tilde{V} = 0 \tag{3.2.15}$$

$$k = \frac{\omega}{c_1} \left[1 + \frac{1}{8} \frac{K^2}{\omega^2} \right], \qquad a = \frac{c_1}{f} \left[1 + \frac{3}{8} \frac{K^2}{\omega^2} \right] \tag{3.2.16}$$

$$\alpha = \frac{K}{2c_1}, \qquad l = \frac{f}{2c_1} \frac{K}{\omega} \tag{3.2.17}$$

These results deserve some comments. Following the anticipated form of the solution, the interface amplitude is exponentially damped both along positive x and y axis. The damping along x is proportional with K and thus a small number. The oscillation along the y-axis is frictionally motivated and will disappear if there is no friction. The friction gives rise to a second sinusoidal component in the current, resulting in the current and interface elevation being slightly out of phase. This effect is treated more carefully in other papers (Martinsen and Weber, 1981). If the friction component is removed, K, l and α are all zero, and we get the familliar internal undamped Kelvin wave solution:

$$\tilde{\xi} = \hat{\xi} e^{-y/a} \cos(kx - \omega t) \tag{3.2.18}$$

$$\tilde{U} = -c_1 \hat{\xi} e^{-y/a} \cos(kx - \omega t) \tag{3.2.19}$$

The damping coefficient perpendicular to the coast is $1/a$, where a is known as the internal, or baroclinic, Rossby radius of deformation (LeBlond and Mysak, 1989).

3.3 Wave energy

The energy associated with our wave system is derived below. A parallell is drawn to the more familiar one-layer case. From LeBlond and Mysak (1989), the energy in one layer surface waves may be expressed as

$$\bar{E}_p = \frac{1}{T} \int_0^T \int_0^\eta g \rho z dz dt \tag{3.3.1}$$

$$\bar{E}_k = \frac{1}{T} \int_0^T \int_{-H}^\eta \frac{1}{2} \rho (u^2 + v^2 + w^2) dz dt \tag{3.3.2}$$

for mean potential and kinetic energy respectively, pr unit area. Here, the effect of surface tension is omitted. The fluid at rest is defined to have zero

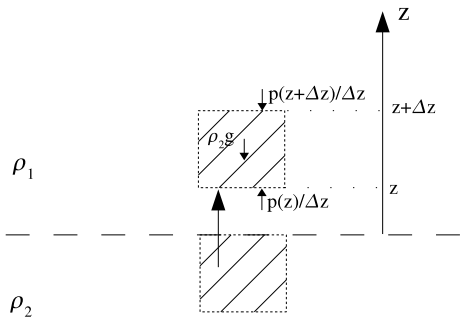

Figure 3.2: *Illustration of a fluid particle, with density ρ_2, unit area and height Δz, displaced in an environment with density ρ_1. Forces acting on the particle are indicated.*

potential energy. $T = 2\pi/\omega$ is wave period, H is fluid depth, η is surface elevation, ρ is fluid density and u, v, w are the three orthogonal current components.

We will soon derive the similar expressions for the energy in a two-layer system. However, first we need to get a better understanding of how potential energy should be interpreted. In the case of surface waves, consider a fluid particle of unit area and height Δz, being displaced a distance η over the surface $z = 0$ at rest. The resultant force per volume in the z-direction acting on this particle is

$$\Sigma F_z = -\rho g + p(\eta)/\Delta z - p(\eta + \Delta z)/\Delta z. \tag{3.3.3}$$

The potential energy of this particle is the integral of the force ΣF_z along the vertical path from $z = \eta$ to the equilibrium height $z = 0$. If pressure differences in the air are neglected, the resulting potential energy for this particle is $\rho g \eta$. When integrating in the vertical and averaging over a wave period we get equation (3.3.1). This is then the total mean potential energy per unit area.

Let us now take a look at figure 3.2 illustrating the similar case in a two-layer fluid. In this scenario, a particle in layer two is displaced in layer one. The forces acting on this particle are the same as in the one layer case. However, the pressure variation in the vertical is here according to the hydrostatic pressure distribution

$$\frac{\partial p}{\partial z} = -\rho_1 g. \tag{3.3.4}$$

The resultant force per volume in the z-direction is now

$$\Sigma F_z = -\rho_2 g - p(z + \Delta z)/\Delta z + p(z)/\Delta z = -\rho_2 g + \rho_1 g = -g_* \rho_2, \tag{3.3.5}$$

when $\Delta z \to 0$. Accordingly, we must substitute $g\rho$ with $g_*\rho_2$ in equation (3.3.1). Obviously we also need to replace η with the interface elevation ξ. As for $\bar{E}_k$, we neglect vertical variations as before, setting $u = \tilde{U}/H_1$. Calculating to second order in wave amplitude, we integrate from 0 to H_1, inserting ρ_1 and setting $v, w = 0$. Inserting from (3.2.13) and (3.2.14), the energy per unit area for our wave system becomes

$$\bar{E}_p = \frac{1}{T}\int_0^T \int_0^{\tilde{\xi}} g_*\rho_2 z dz dt = \frac{1}{4}\rho_2 g_* \hat{\xi}^2 e^{-2(\alpha x + y/a)} \tag{3.3.6}$$

$$\begin{aligned}\bar{E}_k &= \frac{1}{T}\int_0^T \int_0^{H_1} \frac{1}{2}\rho_1(\tilde{U}^2/H_1^2) dz dt \\ &= \frac{1}{4}\rho_1 g_* \hat{\xi}^2 e^{-2(\alpha x + y/a)} \left(1 - \frac{K^2}{4\omega^2}\right).\end{aligned} \tag{3.3.7}$$

Assuming $|\rho_2/\rho_1| \sim 1$, we get the expression for the total mean energy density, correct to $\mathcal{O}(K/\omega)$:

$$\begin{aligned}\bar{E} = \bar{E}_p + \bar{E}_k &= \frac{1}{4}(\rho_1 + \rho_2) g_* \hat{\xi}^2 e^{-2(\alpha x + y/a)} \\ &\approx \frac{1}{2}\rho_1 g_* \hat{\xi}^2 e^{-2(\alpha x + y/a)}.\end{aligned} \tag{3.3.8}$$

The mean energy density for internal waves is proportional to the wave amplitude to the second order, in the same manner as surface waves.

Chapter 4

Nonlinear theory for a straight coast

We have now established theory for an internal Kelvin wave. This wave propagates along a straight coast, bound by rotation and damped by friction. In this chapter we will look at the nonlinear theory regarding this wave motion. Classical Stokes drift theory will be applied, and we will then work on the equations of motion correct to $\mathcal{O}(\epsilon)^2$, to get expressions for the second order flow.

4.1 The Stokes drift

In the most common ocean waves, there is a net particle drift in the direction of wave propagation (see Appendix A). We will in the following apply the theory of Stokes (1847) to our previously derived Kelvin wave, to derive the drift in this wave. As described in Phillips (1980), we may define the Lagrangian velocity $\mathbf{u}_l(\mathbf{a}, t)$ as the velocity of a fluid particle being in $\mathbf{x} = \mathbf{a}$ at $t = 0$. The position of this particle at subsequent times may be written

$$\mathbf{x} = \mathbf{a} + \int_0^t \mathbf{u}_l(\mathbf{a}, t')dt'. \tag{4.1.1}$$

The Eulerian velocity $\mathbf{u}_e(\mathbf{x}, t)$ is the field variable giving the velocity in position $\mathbf{x}$ at time t. Using (4.1.1) this leads to the following:

$$\begin{aligned}\mathbf{u}_l(\mathbf{a}, t) = \mathbf{u}_e(\mathbf{x}, t) &= \mathbf{u}_e\left(\mathbf{a} + \int_0^t \mathbf{u}_l(\mathbf{a}, t')dt', t\right) \\ &= \mathbf{u}_e(\mathbf{a}, t) + \left(\int_0^t \mathbf{u}_l(\mathbf{a}, t')dt'\right) \cdot \nabla_a \mathbf{u}_e(\mathbf{a}, t) + ...,\end{aligned} \tag{4.1.2}$$

using a series expansion (Longuet-Higgins, 1953). From (4.1.2) it is evident that the Lagrangian and Eulerian terms are equal to the first order. We

assume wave motion and average equation (4.1.2) over a wave period. Neglecting third order terms we arrive at the approximated Stokes drift solution:

$$\bar{\mathbf{u}}_l(\mathbf{a},t) = \bar{\mathbf{u}}_e + \overline{\left(\int_0^t \mathbf{u}_e(\mathbf{a},t')dt'\right)\cdot\nabla_a\mathbf{u}_e(\mathbf{a},t)} \equiv \bar{\mathbf{u}}_e + \bar{\mathbf{u}}_s(\mathbf{a},t) \tag{4.1.3}$$

The wave motion is not contained in the Eularian mean current $\bar{\mathbf{u}}_e$. However, the term is not necessarily zero, as will be shown later on. Let us now try to relate the Stokes drift term $\bar{\mathbf{u}}_e$ to the first order flux vector $\tilde{\mathbf{U}} = \tilde{U}\mathbf{i}$. We assume that $|\bar{\mathbf{u}}_e| \ll |\mathbf{u}_e|$. Accordingly, we only include the wave motion part of $\mathbf{u}_e$ when evaluating the Stokes drift term. Neglecting vertical variations we set $\mathbf{u}_e = \tilde{\mathbf{U}}/H_1$ and $\bar{\mathbf{U}}_s = \bar{\mathbf{u}}_s H_1$. Using (3.2.14) in (4.1.3), the Stokes drift solution for this problem is then

$$\begin{aligned}\bar{\mathbf{U}}_s &= H_1\overline{\left(\int_0^t \tilde{\mathbf{U}}/H_1 dt'\right)\cdot\nabla\tilde{\mathbf{U}}/H_1} = \frac{1}{H_1}\overline{\int_0^t \tilde{U}dt'\cdot\tilde{U}_x}\mathbf{i} \\ &= \frac{c_1}{2H_1}\,\hat{\xi}^2\, e^{-2(\alpha x + y/a)}\left(1 - \frac{3}{8}\frac{K^2}{\omega^2}\right)\mathbf{i}. \end{aligned} \tag{4.1.4}$$

There is no Stokes component normal to the wall; the Stokes drift is always in the direction of wave propagation. As the first order wave component $\tilde{V}$ is shown to be zero, there cannot exist a Stokes component in this direction.

How does this result connect to the wave energy? Inserting (4.1.4) in (3.3.8) we get the elegant solution

$$\bar{E} = \frac{1}{2}\rho_1 g_* \hat{\xi}^2 e^{-2(\alpha x + y/a)} = \rho_1 c_1 \bar{U}_s. \tag{4.1.5}$$

The mean internal wave energy is thus the product of the Stokes flux $\rho_1\bar{U}_s$ and the internal phase speed c_1. This result is equivalent to one layer theory, as shown in Phillips (1980).

4.2 Equations to $\mathcal{O}(\epsilon)^2$

In this section we derive the equations of motion and continuity equations, valid to $\mathcal{O}(\epsilon)^2$ and averaged over a wave period. This equation set may then be used to extract the mean properties of the internal Kelvin wave derived earlier.

The expansions (2.2.14) are inserted in equations (2.2.11)-(2.2.13), keeping terms up to $\mathcal{O}(\epsilon)^2$. We neglect all variations in the vertical, so the convective terms are approximated as

$$\int_0^{H_1} u_1^2 dz = \int_0^{H_1}\left(\frac{U_1}{H_1}\right)^2 dz = \frac{1}{H_1}\tilde{U}^2.$$

Note that as $\tilde{V} = 0$ (from section 3.2), u_1^2 is the only convective term that makes a contribution. The moment equations now become:

$$\frac{\partial}{\partial t}(\tilde{U} + \bar{U}) - f\bar{V} - c_1^2 \frac{\partial}{\partial x}(\tilde{\xi} + \bar{\xi}) + K(\tilde{U} + \bar{U}) = -\frac{g_*}{2}\frac{\partial(\tilde{\xi}^2)}{\partial x} - \frac{1}{H_1}\frac{\partial(\tilde{U}^2)}{\partial x} \tag{4.2.1}$$

$$\frac{\partial \bar{V}}{\partial t} + f(\tilde{U} + \bar{U}) - c_1^2 \frac{\partial}{\partial y}(\tilde{\xi} + \bar{\xi}) + K\bar{V} = -\frac{g_*}{2}\frac{\partial(\tilde{\xi}^2)}{\partial y}. \tag{4.2.2}$$

The forcing in our problem is a monochromatic wave, with constant frequency ω and amplitude ξ at $x = 0$, and a purely horizontal damping. We average equations (4.2.1)-(4.2.2) over a wave period $T = 2\pi/\omega$, removing all linear first order terms. Due to the quasi-stationarity of the first order motion, we assume that the mean second order motion is constant in time. Thus the time derivatives disappear, and also $\overline{(\bar{\cdot})} = \bar{\cdot}$. The moment and continuity equations are concludingly:

$$-f\bar{V} - c_1^2 \frac{\partial \bar{\xi}}{\partial x} + K\bar{U} = -\frac{g_*}{2}\frac{\partial \overline{(\tilde{\xi}^2)}}{\partial x} - \frac{1}{H_1}\frac{\partial \overline{(\tilde{U}^2)}}{\partial x} \tag{4.2.3}$$

$$f\bar{U} - c_1^2 \frac{\partial \bar{\xi}}{\partial y} + K\bar{V} = -\frac{g_*}{2}\frac{\partial \overline{(\tilde{\xi}^2)}}{\partial y} \tag{4.2.4}$$

$$\frac{\partial \bar{U}}{\partial x} + \frac{\partial \bar{V}}{\partial y} = 0. \tag{4.2.5}$$

4.3 The mean mass transport

We will now attempt to solve the equations (4.2.3)-(4.2.5). The solution should give expressions on the mass transport terms $\bar{U}$ and $\bar{V}$.

4.3.1 An intuitive attempt

From the first order solution we have $\tilde{V} = 0$. We first assume that $\bar{V} = 0$ too, simplifying our second order equation. $\bar{\xi}$ is eliminated by taking the curl of the momentum equations, meaning that we subtract the y-derivative of the momentum equation in the x-direction from the x-derivative of the y-momentum equation. Making use of (3.2.14) the expression becomes, correct to $\mathcal{O}(K/\omega)$:

$$\begin{aligned}\left(f\frac{\partial}{\partial x} - K\frac{\partial}{\partial y}\right)\bar{U} &= \frac{1}{H_1}\frac{\partial^2}{\partial x \partial y}\overline{(\tilde{U}^2)} \\ &= \frac{1}{H_1}\frac{\partial^2}{\partial x \partial y}\left({c_1}^2 \hat{\xi}^2 e^{-2(\alpha x + y/a)}\frac{1}{2}\right) \\ &= \frac{Kf}{H_1}\hat{\xi}^2 e^{-2(\alpha x + y/a)}.\end{aligned}$$

Now we see the contours of a problem: From (4.2.5) $\partial\bar{U}/\partial x = 0$. Integrating the above expression with respect to y once and then differentiating with respect to x, we get a $\partial\bar{U}/\partial x$-term on the left hand side. On the right hand side there will still be a $e^{-2(\alpha x+y/a)}$-term which is not zero. Accordingly, although $\tilde{V}$ is zero, $\bar{V}$ must be nonzero (as long as $K \neq 0$). There must be a mean flux perpendicular to the coast at some point. At $y = 0$ this flux must also be zero, but away from the wall it has some value to be determined.

The above result could be anticipated earlier. We found in the previous chapter that the wave amplitudes along x were decaying spatially as a result of friction. The drift in the wave would then decay accordingly. The decay in volume transport along the coast must be compensated by an outflow elsewhere, and the only possible direction is normal to the coast. As we already integrated in the vertical, the flow can only propagate outwards, giving $\bar{V} \neq 0$.

4.3.2 The stream function solution

In the previous subsection it is shown that $\bar{V} \neq 0$ when the friction coefficient K is nonzero. The drift thus follows a two-dimentional pattern (remember that vertical changes are discarded). A common method in fluid mechanics for describing two-dimensional flow, is to introduce the stream function Ψ, defined as follows:

$$\bar{U} = -\frac{\partial\Psi}{\partial y}, \qquad \bar{V} = \frac{\partial\Psi}{\partial x}. \tag{4.3.1}$$

From the definition of Ψ, the continuity equation (4.2.5) is exactly satisfied. The curl of the flux vector reveals another convenient relation:

$$\nabla \times (\bar{U}\mathbf{i} + \bar{V}\mathbf{j}) = \left(-\frac{\partial\bar{U}}{\partial y} + \frac{\partial\bar{V}}{\partial x}\right)\mathbf{k} = \nabla^2\Psi\,\mathbf{k}. \tag{4.3.2}$$

So, once again we have a look at the second order equations, and take the curl as before. Introducing the stream function this time however, we get a somewhat different result:

$$\begin{aligned} K\nabla^2\Psi &= \frac{1}{H_1}\frac{\partial^2}{\partial x\partial y}\overline{(\tilde{U}^2)} \\ &= 2g_*\frac{\alpha}{a}\hat{\xi}^2 e^{-2(\alpha x+y/a)}\left(1 - \frac{1}{2}\frac{K^2}{\omega^2}\right). \end{aligned} \tag{4.3.3}$$

There is a singular nature in equation (4.3.3). As α is proportional to K, setting $K = 0$ would result in a $0 = 0$ equation. When there is no friction, this method of solution may accordingly not be applied.

Some boundary conditions are needed on Ψ. At $y = 0$ the coast-normal

component must be zero. Further, the solution must remain regular far away from the origin. We state the following:

$$\bar{V}|_{y=0} = \left.\frac{\partial \Psi}{\partial x}\right|_{y=0} = 0, \qquad \Psi|_{x,y\to\infty} \sim \text{regular}. \tag{4.3.4}$$

As we have no explicit boundary condition in x except the regularity condition, a guessed form of the solution is

$$\Psi = [f_h(y) + f_p(y)]\, e^{-2\alpha x}. \tag{4.3.5}$$

This is a rather strong assumption. One would maybe expect a different x-dependency. As the Stokes drift is decaying along the coast, the loss in wave momentum should maybe be compensated by an increasing Eulerian mean flow. However, due to the bulk friction, such a rigid transition is not necessarily present.

The homogeneous solution f_h satisfies the Laplace equation

$$\nabla^2[f_h(y)e^{-2\alpha x}] = 0$$

giving the general solution

$$f_h(y) = A_1 \sin(2\alpha y) + A_2 \cos(2\alpha y). \tag{4.3.6}$$

The particular solution $f_p(y)$ is found from (4.3.3):

$$\begin{aligned}\nabla^2[f_p(y)e^{-2\alpha x}] &= [f_p(y)_{yy} + 4\alpha^2 f_p(y)]e^{-2\alpha x} \\ &= \frac{2g_*}{K}\frac{\alpha}{a}\,\hat{\xi}^2\, e^{-2(\alpha x + y/a)}\left(1 - \frac{1}{2}\frac{K^2}{\omega^2}\right),\end{aligned} \tag{4.3.7}$$

and by inspection a guessed solution has the form

$$f_p(y) = A_3 e^{-2y/a}. \tag{4.3.8}$$

Using (4.3.8), inserting from the dispersion relations (3.2.16) and (3.2.17) and expanding to order $\mathcal{O}(K/\omega)^2$ as before we get:

$$\begin{aligned}(4/a^2 + 4\alpha^2)A_3 e^{-2y/a} &= \frac{c_1}{H_1}\frac{1}{a}\,\hat{\xi}^2\left(1 - \frac{1}{2}\frac{K^2}{\omega^2}\right)e^{-2y/a} \\ \Rightarrow A_3 &= \frac{1}{4}\frac{c_1}{H_1}\,a\,\hat{\xi}^2\left(1 - \frac{1}{4}\frac{K^2}{f^2} - \frac{1}{2}\frac{K^2}{\omega^2}\right).\end{aligned} \tag{4.3.9}$$

An important comment is needed about the ordering here. As a result of the derivations, the term $(K/f)^2$ appeared. Since we have assumed that we are far from the equator, between $\phi = \{60°, 90°\}$ say, the Coriolis parameter f is in the range $\{1.26,1.45\}$*10^{-4}s^{-1}. The driving frequency has its origin

in the M_2-tidal component with a frequency $\omega \approx 1.41{*}10^{-4}\mathrm{s}^{-1}$. From this K/f and K/ω are of the same order of magnitude, and will be regarded as such in all order of magnitude derivations.

Moving on, we can now use (4.3.4) to determine A_2:

$$\left.\frac{\partial \Psi}{\partial x}\right|_{y=0} = -2\alpha[A_2 + A_3]e^{-2\alpha x} = 0$$
$$\Rightarrow A_2 = -A_3 = \frac{1}{4}\frac{c_1}{H_1}\, a\, \hat{\xi}^2 \left(1 - \frac{1}{4}\frac{K^2}{f^2} - \frac{1}{2}\frac{K^2}{\omega^2}\right). \tag{4.3.10}$$

We do not have enough information to determine the last free constant, and for now we just redefine it as $A_1' \equiv A_1/A_2$.

The sinusoidal terms are the next target of investigation. The term αa is proportional to K/f and must be small. Since we are not interested in solutions far away from the coast, we may set $y/a \sim \mathcal{O}(1)$. Utilizing a series expansion following these assumptions, we get

$$\sin(2\alpha y) = \sin\left[2(\alpha a)\frac{y}{a}\right] \approx 2(\alpha a)\frac{y}{a}\left[1 - \frac{2}{3}(\alpha a)^2\frac{y^2}{a^2}\right]$$
$$= \frac{y}{a}\frac{K}{f}\left[1 - \frac{1}{6}\frac{y^2}{a^2}\frac{K^2}{f^2} + \frac{3}{8}\frac{K^2}{\omega^2}\right] \tag{4.3.11}$$
$$\cos(2\alpha y) = \cos\left[2(\alpha a)\frac{y}{a}\right] \approx 1 - 2(\alpha a)^2\frac{y^2}{a^2}$$
$$= 1 - \frac{1}{2}\frac{y^2}{a^2}\frac{K^2}{f^2}. \tag{4.3.12}$$

Now we can gather terms to obtain a solution for Ψ:

$$\Psi = A_3\left[e^{-2y/a} - \cos(2\alpha y) - A_1'\sin(2\alpha y)\right]e^{-2\alpha x}$$
$$\approx \frac{c_1}{4H_1}\, a\, \hat{\xi}^2 e^{-2\alpha x}\left[e^{-2y/a} - 1 + \frac{1}{2}\frac{y^2}{a^2}\frac{K^2}{f^2} - A_1'\frac{y}{a}\frac{K}{f}\right]\left(1 - \frac{1}{4}\frac{K^2}{f^2} - \frac{1}{2}\frac{K^2}{\omega^2}\right). \tag{4.3.13}$$

From (4.3.1) we may finally write down the solution for $\bar{U}$ and $\bar{V}$:

$$\bar{U} = \frac{c_1}{2H_1}\hat{\xi}^2 e^{-2\alpha x}\left[e^{-2y/a} - \frac{1}{2}\frac{y}{a}\frac{K^2}{f^2} + \frac{A_1'}{2}\frac{K}{f}\right]\left(1 - \frac{1}{4}\frac{K^2}{f^2} - \frac{1}{2}\frac{K^2}{\omega^2}\right) \tag{4.3.14}$$

$$\bar{V} = \frac{c_1}{2H_1}\hat{\xi}^2 e^{-2\alpha x}\left[1 - e^{-2y/a} - \frac{1}{2}\frac{y^2}{a^2}\frac{K^2}{f^2} + A_1'\frac{y}{a}\frac{K}{f}\right]\frac{K}{2f}\left(1 - \frac{1}{4}\frac{K^2}{f^2} - \frac{1}{8}\frac{K^2}{\omega^2}\right). \tag{4.3.15}$$

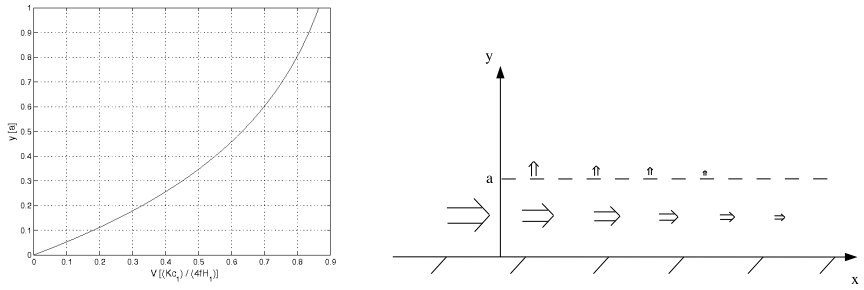

Figure 4.1: *The mean flow illustrated. To the left, $\bar{V}$ is plotted against y. Note the scaled axis, see equation (4.3.17). To the right is an illustration of the drift resulting from the wave system indicated in figure 3.1. The drift is decaying alongshore, due to friction. A gradually decreasing outward drift is compensating the loss in volume transport.*

If we neglect $\mathcal{O}(K/\omega)^2$ and set $A_1' = 0$, these expressions simplify to

$$\bar{U} = \frac{c_1}{2H_1}\hat{\xi}^2\, e^{-2(\alpha x + y/a)} \tag{4.3.16}$$

$$\bar{V} = \frac{c_1}{2H_1}\hat{\xi}^2\, e^{-2\alpha x}(1 - e^{-2y/a})\frac{K}{2f}. \tag{4.3.17}$$

Now this is an interesting result. The alongcoastal transport is a positive quantity, which is expected. The spatial dependence is similar to that of the first order solution, although changed by a factor 2. The wave averaged flow is accordingly damped on half the scale than the first order wave motion. The transport along x is exactly the same as the Stokes drift U_s derived in (4.1.4). The component normal to the wall however is somewhat different. Firstly it is one order of magnitude (in the order K/ω) smaller than the along-coastal component. Furthermore it increases steadily from zero at the coast and out to $y = a$, i.e. at the outermost range where the Kelvin wave is of significance. For $y \gg a$ the approximated series expansions for $\sin(2\alpha y)$ and $\cos(2\alpha y)$ are not valid, and thus the solution does not apply there.

Let us look at the variation in $\bar{V}$ normal to the coast. Figure 4.1 shows a plot of $\bar{V}$ against y, along with an illustration of the drift. We see from the plot that $\bar{V}$ is closing in on its maximum value at $y = a$. Inserting this y-value in equation (4.3.17), we get

$$\bar{V}|_{y=a} = 0.86 * \bar{V}_{max}. \tag{4.3.18}$$

The drift illustration is merely to show how the alongshore drift is decaying, along with a gradually decaying outward flow normal to the coast.

A comment should be made on the constant A_1'. From equation (4.3.13) it gives a sinusoidal contribution to the flow, with variation over quite a long scale. Its amplitude may mathematically speaking take any value, however the physics of our problem hints toward small amplitudes, and by inserting a new boundary condition, say $\bar{U}|_{y\to\infty} = 0$ and neglecting $\mathcal{O}(K/\omega)^2$ we are forced to set $A_1' = 0$.

4.3.3 The total transport

The wave propagating around the basin, will cause a transport of mass in accordance with (4.3.16), correct to $\mathcal{O}(K/\omega)$. By integrating $\bar{U}$ from $y = 0$ to $2a$ we get an approximate expression for the total volume transport associated with the wave:

$$\begin{aligned}\int_0^{2a} \bar{U}(x,y)dy &= \int_0^{2a} \frac{c_1}{2H_1}\hat{\xi}^2 e^{-2(\alpha x + y/a)}dy \\ &= \frac{g_*}{4f}\hat{\xi}^2 e^{-2\alpha x}(1-e^{-4}). \end{aligned} \tag{4.3.19}$$

This equation may be somewhat misleading, as it would seem that decreasing the rotation results in larger transport. This is not necessarily the case, as $\hat{\xi}$ is dependent on the rotation as well. Remember that this is simply the amplitude in origo. In our model $\hat{\xi}$ is a freely determinable constant, but altering f without reevaluating $\hat{\xi}$ is not physical. Knowing the wave amplitude from measurements, however, justifies using (4.3.19) to estimate the mean volume transport in the wave.

The integration limit $2a$ is chosen to illustrate that outside this limit there is practically no mass transport present. If we choose infinity as integration limit, the e^{-4} term will disappear. This will then give an increase in transport of no more than 2%.

4.4 The mean interface

Associated with the mean second order drift is a mean displacement of the interface $\bar{\xi}$. Anticipating the form of this elevation, or even some condition at $y = 0$, is far from trivial. We need to dive into the equations once again, setting $A_1' = 0$ according to the new boundary condition $\bar{U}|_{y\to\infty} = 0$. Defining the right hand side of (4.2.3) as RHS1, we write:

$$c_1^2 \frac{\partial \bar{\xi}}{\partial x} = -f\bar{V} + K\bar{U} - \text{RHS1}. \tag{4.4.1}$$

Inserting from (3.2.13) and (3.2.14), RHS1 is calculated:

$$\begin{aligned}\text{RHS1} &= -\frac{\partial}{\partial x}\left[\frac{g_*}{2}\,\hat{\xi}^2\,e^{-2(\alpha x+y/a)}\frac{1}{2}+\frac{1}{H_1}c_1^2\,\hat{\xi}^2\,e^{-2(\alpha x+y/a)}\frac{1}{2}\left(1-\frac{1}{2}\frac{K^2}{\omega^2}\right)\right]\\ &= \frac{3}{4}\frac{c_1K}{H_1}\,\hat{\xi}^2\,e^{-2(\alpha x+y/a)}\left(1-\frac{1}{3}\frac{K^2}{\omega^2}\right). \qquad (4.4.2)\end{aligned}$$

After lengthy algebra and series expansions, the following is obtained from inserting (4.3.14), (4.3.15) and (4.4.2) into (4.4.1):

$$\begin{aligned}c_1^2\frac{\partial\bar{\xi}}{\partial x} = -\frac{Kc_1}{4H_1}\,\hat{\xi}^2\,e^{-2\alpha x}\Bigg[1-\frac{K^2}{4f^2}-\frac{K^2}{8\omega^2}+\frac{y}{a}\frac{K^2}{f^2}-\frac{y^2}{a^2}\frac{K^2}{2f^2}+\cdots\\ +\left(\frac{3K^2}{4f^2}+\frac{K^2}{8\omega^2}\right)e^{-2y/a}\Bigg]\end{aligned}$$

Integrating this equation, it is a simple exercise to show that:

$$\begin{aligned}\bar{\xi} = \frac{1}{4H_1}\,\hat{\xi}^2\,e^{-2\alpha x}\Bigg[1-\frac{K^2}{4f^2}-\frac{K^2}{8\omega^2}+\frac{y}{a}\frac{K^2}{f^2}-\frac{y^2}{a^2}\frac{K^2}{2f^2}+\cdots\\ +\left(\frac{3K^2}{4f^2}+\frac{K^2}{8\omega^2}\right)e^{-2y/a}\Bigg]. \qquad (4.4.3)\end{aligned}$$

A comment is needed about the integration process. In general, the solution for $\bar{\xi}$ would contain a $\bar{\xi}_0(y)$-term, being an arbitrary function of y. However, by inspection of (4.2.4) it is clear that $\partial\bar{\xi}/\partial y$ cannot avoid containing the term $e^{-2\alpha x}$, leading to the only conclusion that $\partial\bar{\xi}_0/\partial y = 0$, and $\bar{\xi}_0$ accordingly being a constant. Furthermore we want the interface to approach zero far away from our origo in accordance with the sketched figure 2.1, hence we set $\bar{\xi}_0 = 0$.

Looking at (4.4.3) it is clear that if we neglect $\mathcal{O}(K/\omega)^2$, we loose all information of y-dependence. The resulting expression is then simply

$$\bar{\xi} = \frac{1}{4H_1}\,\hat{\xi}^2\,e^{-2\alpha x}. \qquad (4.4.4)$$

In case there is no friction, $\bar{\xi}$ becomes a constant, and interestingly independent of y even for higher order calculations.

4.5 Radiation stress

Longuet-Higgins and Stewart introduced theory on radiation stress in a series of papers around the year 1960. Radiation stress is excess momentum flux due to the presence of waves, and the theory is summarized in Phillips (1980). In the following we will try to relate their results to the two layer system

currently under investigation.

Assume an incompressible one layer system, in hydrostatic equilibrium with no friction or Coriolis force. The horizontal momentum equation may in this system be formulated on the simple form

$$\frac{\partial}{\partial t}(\rho u_i) + \frac{\partial}{\partial x_j}(\rho u_i u_j + p\delta_{ij}) + \frac{\partial}{\partial z}(\rho u_i w) = 0, \qquad i,j = 1,2. \tag{4.5.1}$$

Here x_1, x_2 represents x, y respectively. Let us assume monochromatic wave motion. Then we may eliminate linear terms by averaging over one wave period. Integrating equation (4.5.1) in the vertical, averaging and neglecting third order terms, we get the steady-state relation

$$\frac{\partial S_{ij}}{\partial x_j} = -\rho g(d+h)\frac{\partial h}{\partial x_i}, \tag{4.5.2}$$

where

$$S_{ij} = -\tau_{ij} + E\,\frac{c_g}{c}\frac{k_i k_j}{k^2} + \frac{E}{2}\left(\frac{2c_g}{c} - 1\right)\delta_{ij}. \tag{4.5.3}$$

In the above derivation, taken directly from Phillips, h is surface elevation, d is fluid depth, p is pressure, E is wave energy pr unit area, c_g is group velocity and c is phase speed of the surface wave with wave number components k_1, k_2. S_{ij} is called the excess momentum flux tensor, containing an integrated turbulent Reynolds stress term τ_{ij}, and the remainder being the sought radiation stress.

Now let us look at equations (4.2.3) and (4.2.4). Denoting the right hand sides as RHS1 and RHS2 we insert from (3.2.13) and (3.2.14). Neglecting terms of $\mathcal{O}(K/\omega)^2$, we may write

$$\text{RHS1} = -\frac{\partial}{\partial x}\left(\frac{3}{4}\,g_*\,\hat{\xi}^2\,e^{-2(\alpha x + y/a)}\right) \tag{4.5.4}$$

$$\text{RHS2} = -\frac{\partial}{\partial y}\left(\frac{1}{4}\,g_*\,\hat{\xi}^2\,e^{-2(\alpha x + y/a)}\right). \tag{4.5.5}$$

The upper layer second order momentum balance then reveals, inserting the Stokes expression (4.1.4) and the energy (3.3.8):

$$\begin{aligned} -f\bar{V} - c_1^2\frac{\partial \bar{\xi}}{\partial x} + K\bar{U} &= -\frac{\partial}{\partial x}\left(\frac{3}{4}\,g_*\,\hat{\xi}^2\,e^{-2(\alpha x + y/a)}\right) \\ &= -\frac{\partial}{\partial x}\left(\frac{3}{2}\bar{U}_s c_g\right) = -\frac{\partial}{\partial x}\left(\frac{3}{2}\frac{\bar{E}}{\rho_1}\right) \end{aligned} \tag{4.5.6}$$

$$\begin{aligned} f\bar{U} - c_1^2\frac{\partial \bar{\xi}}{\partial y} + K\bar{V} &= -\frac{\partial}{\partial y}\left(\frac{1}{4}\,g_*\,\hat{\xi}^2\,e^{-2(\alpha x + y/a)}\right) \\ &= -\frac{\partial}{\partial y}\left(\frac{1}{2}\bar{U}_s c_g\right) = -\frac{\partial}{\partial y}\left(\frac{1}{2}\frac{\bar{E}}{\rho_1}\right) \end{aligned} \tag{4.5.7}$$

Hence, the momentum balance involves divergence of wave energy on the right hand side. How does this relate to the radiation stress term from before? Let us assume that the wave is propagating parallell to the coast, and $c_g = c$. This is the case in our model. Then $k_2 = 0$, and thus equation (4.5.3) is reduced to the following:

$$S_{11} + \tau_{11} = (3/2)E \tag{4.5.8}$$

$$S_{22} + \tau_{22} = (1/2)E \tag{4.5.9}$$

Inserting in (4.5.2) we get

$$\rho g(d+h)\frac{\partial h}{\partial x} - \frac{\partial \tau_{11}}{\partial x} = -\frac{\partial}{\partial x}\left(\frac{3}{2}E\right) \tag{4.5.10}$$

$$\rho g(d+h)\frac{\partial h}{\partial y} - \frac{\partial \tau_{22}}{\partial y} = -\frac{\partial}{\partial y}\left(\frac{1}{2}E\right) \tag{4.5.11}$$

Let us include the Reynold stress tensor terms in the KU, KV terms, and remember that there is no Coriolis force in the one-layer equations. Then we realize that the one-layer equations (4.5.10) and (4.5.11) are similar to our two-layer equations (4.5.6) and (4.5.7). The radiation stress theory is accordingly applicable to the two layer system discussed in the rest of this thesis.

Chapter 5

Modelling a theoretical basin

Up to now we have looked at wave motion along a straight wall in a semi-infinite ocean. We have derived expressions for the first order wave motion and dispersion relation. The nonlinear mass transport terms along and normal to the wave motion have been derived. In this chapter these results will be applied to a more closed geometry.

5.1 The mean wave-induced circulation in a semi-enclosed basin

Let us first look at a hypothetical semi-enclosed basin, and discuss how the wave pattern develop here. Consider a basin on the northern hemisphere with a narrow opening, as illustrated in figure 5.1. We denote the walls of the inner basin as A,B,C,D as shown. At the basin entrance there is a

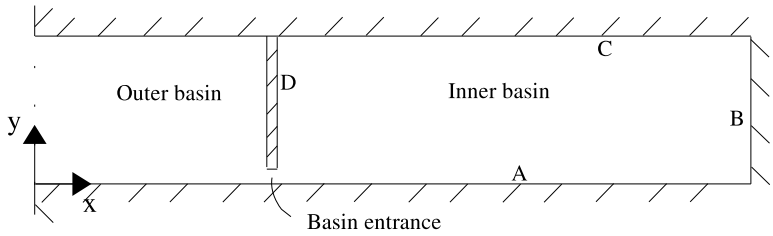

Figure 5.1: *Sketch of the basin. Walls are shown by tilted lines.*

sill. The density distribution inside the basin is approximated as a two-layer model, with a deep lower layer and upper layer depth similar to sill depth.

Outside the basin the water is homogenous. We assume barotropic wave motion of constant frequency and amplitude here. The small cross-sectional area at the basin entrance restrict the volume fluxes into the basin. Change

in surface amplitudes inside the basin may accordingly be delayed compared to the barotropic wave motion outside. The flow through the entrance may reach super-critical velocities (Bergh, 2004). However, at some point inside the basin the flow will become subcritical. From this point onward, the oscillating pressure gradients may give rise to internal Kelvin waves of potentially much larger amplitudes than the surface amplitudes. Let us assume that the basin is much longer than one wavelength, and much wider than the internal Rossby radius a defined in equation (3.2.16). We then have conditions in favour of an internal Kelvin wave solution along wall A, as shown in equation (3.2.14).

5.1.1 Neglecting friction

Let us assume that there is an internal Kelvin wave propagating along wall A, not influenced by friction. Due to the rotation of the earth, and as we are on the northern hemisphere, the wave is trapped with the wall on its right. At the A/B corner, the wave is given no option but to continue its propagation along wall B. Eventually the wave have propagated around the whole basin.

This internal Kelvin wave induce a mean drift, approximately given by (4.3.16). As the wave is propagating around the whole basin, the wave induced current must follow the same pattern. At the D/A corner it is not trivial to describe what happens in detail. However mass must be conserved in this corner. As we allow no net flow into the basin, i.e. through the basin entrance, the downward drift toward wall A must exactly compensate the rightward drift out of the D/A corner. It seems that we have obtained a system of a closed quasi-stationary circulation in the basin.

In this discussion we have omitted a central problem in this model setup. If there is no friction, the wave will re-enter wall A after propagating around the basin. However, as there already is a wave propagating here, this wave will be superimposed on the "old" wave. The resulting interference is dependent on the internal phase speed, as well as the circumference of the basin. We will not look more into this effect here. Let us instead study the more realistic scenario where friction will prevent the wave from reaching all the way around the basin:

5.1.2 Including friction

The friction leads to a spatial damping of the wave amplitudes. This leads to a decay of the wave drift, as presented in equation (4.3.16). If the circumference of the basin is large enough or the friction strong enough, the wave will not reach around the entire basin. Then the wave-induced along-shore

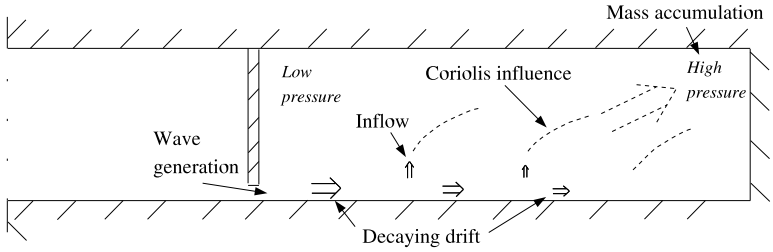

Figure 5.2: *Sketch of the drift in the basin. The inflow, due to the decay in the drift, is affected by the Coriolis force and deflected to the right. In the top right corner, the indicated mass accumulation and corresponding high pressure is indicated.*

current will approach zero. Thus there cannot be a circulation in the basin due to Stokes drift alone.

The reduction in wave drift is compensated by a current component normal to the wall, as discussed in subsection 4.3.2; see figure 5.2. Directed toward the interior of the basin, this current will be affected by the Coriolis force, and accordingly deflected toward the right. It is reasonable to believe that there will be some accumulation of mass along the top right part of the basin. A high pressure zone will develop, forcing the flow back toward the interior of the basin in some way. Due to the influence of the Coriolis force, the system should eventually establish itself in geostrophic balance. The flow would follow the isobars around the high pressure corner, and down wall D; see figure 5.1. There must be conservation of mass in corner D/A, and we conclude that there is still a closed circulation in the basin. However, the flow pattern in the interior is not fully known.

In the next section a numerical model will be applied. We first want to verify the generation of an internal Kelvin wave in such a system as described above. Next we will attempt to construct a model run, to show the drift pattern in the interior in the case of friction.

5.2 A model run

We will in this section apply a numerical model, in order to test the results from the discussion of the previous section. A linear model is provided by professor Bjørn Gjevik at the Department of Mathematics, University of Oslo. Details of the model are described in Appendix B. We here outline that this is a linear two-layer model solving for vertically integrated fluxes of mass in each layer, in addition to surface and interface elevations. These

equations correspond to the previously derived equations (3.2.1)-(3.2.3). We apply a rectangular depth-matrix, and formulate the necessary boundary conditions. In addition, we specify values for the friction coefficient K, upper layer thickness H_1, relative density difference $\Delta\rho/\rho$, gravity g, forcing frequency ω and Coriolis parameter f.

5.2.1 Modelling the wave in a semi-enclosed box

In order to reconstruct the scenario from section 5.1, we introduce a bottom topography as sketched in figure 5.3. To make it simple, we let the basin shape be strictly rectangular, and separate the inner and outer basins by a wall with a small opening in the D/A corner. The depth is 200 m everywhere

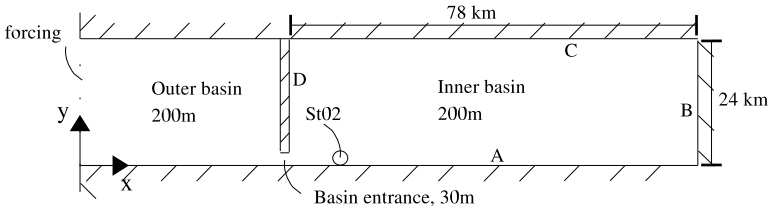

Figure 5.3: *Sketch of simulation area. Forcing is applied along the leftmost open border. Station 02 (St02) is just inside the inner basin.*

except at the narrow opening, where it is 30 m. The inner box is 78 km long and 24 km wide. At the open boundary we formulate the forcing as weak barotropic oscillations, with surface amplitude 5.22 cm and no flow into or out of the simulation area.

The input parameters chosen are presented in table 5.1 and explained in the following. The Coriolis parameter is given by equation (2.1.2). As we intend to discuss this in relation to an arctic fjord, we take $\phi = 77.8°$. K is chosen from $K/\omega = 0.1$, using the previously derived condition (3.2.11). ω is the frequency of the tidal M_2 component with a period of 12.4 hours. H_1 is intended to be the same as basin entrance depth, but due to numerical instabilities, the upper layer thickness must be reduced with 5 m. With this

Parameter	K [s^{-1}]	H_1 [m]	$\Delta\rho/\rho$	g [m/s^2]	ω [s^{-1}]	f [s^{-1}]
Value	1.4e-5	25	0.001	9.81	1.41e-4	1.42e-4

Table 5.1: *Input parameters in the model. K is friction coefficient, H_1 upper layer thickness, $\Delta\rho/\rho$ relative density difference, g gravity, ω frequency of forcing and f is the Coriolis parameter.*

Parameter	Expression	Value
c_1	$\sqrt{gH_1\Delta\rho/\rho}$	0.50 m/s
a	c_1/f	3.5 km
λ	$2\pi/k = 2\pi c_1/\omega$	22 km
α	$K/2c_1$	1.4e-5 m^{-1}

Table 5.2: *Calculated parameters, using values from table 5.1 and expressions from section 3.2.* c_1 *is internal phase speed,* a *internal Rossby radius,* λ *wavelength,* α *horisontal damping coefficient in the direction of wave propagation.*

choice of upper layer thickness, the upper layer is much thinner than the lower layer of thickness 175m. We accordingly assume that the motion in the lower layer is negligable.

Based on results from chapter 3, the properties presented in table 5.2 are calculated. Here λ is wavelength with wave number k. From this we see that the dimension of the inner basin is about 3.5 wavelengths and 6.9 times the internal Rossby radius. Hence, the size of the basin is several times the size of one wave.

Two runs were done with this setup. One where K is set to zero, and the other with K as tabulated; see figures 5.4 and 5.5, respectively, for a plot of the interface amplitude after 119 hours of simulation. With this choice of simulation time, the wave has travelled around almost the entire basin, and a quasi-steady state is reached at wall A. The x and y axis correspond to those of figure 5.3. A plot of surface amplitudes for the run without friction is presented in figure 5.6, choosing 109 hours of simulation time for presentational purposes. A timeseries of surface elevation at station 02 is presented in figure 5.7.

The figures show an internal wave trapped against the wall, with amplitudes decaying towards the center of the basin. The interface amplitudes are of order 10 m and much larger than the surface wave amplitudes of order 0.1 m. The wavelength is comparable to the calculated value for an internal Kelvin wave (see table 5.2), and the scale of the damping normal to the wall is much smaller than the width of the basin. An along-coastal decay in amplitude is evident in the case with friction. With our particular choice for K, the wave does not seem to be able to reach around the entire basin.

We note the development of an internal wave propagating outside the basin entrance. This wave is of similar amplitude as the one inside the basin. The

existence of this wave is a consequence of model simplicity, as the density distribution is modelled in the same way outside and inside the basin entrance. In a more realistic simulation, the water outside the basin would probably be more homogenous, and not necessarily support internal waves.

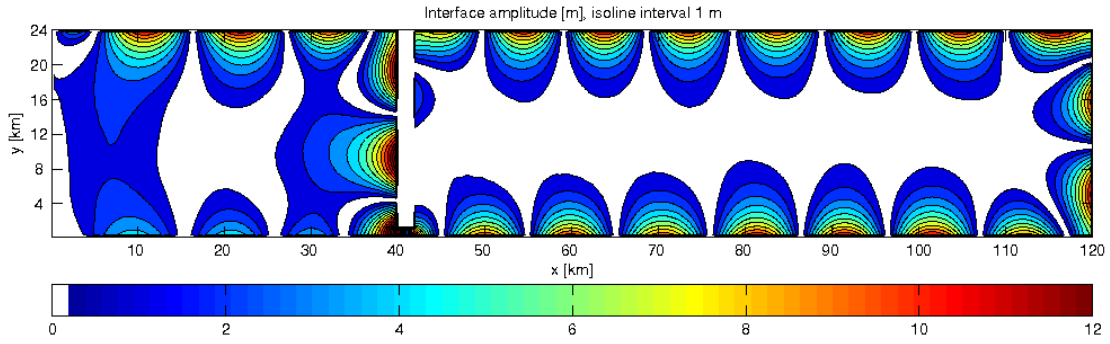

Figure 5.4: *Absolute value of interface amplitudes after 119 hrs simulation time; run without friction. 1 m isolines. Left boundary is open. There is a constriction at x=40 km with an opening by the lower wall.*

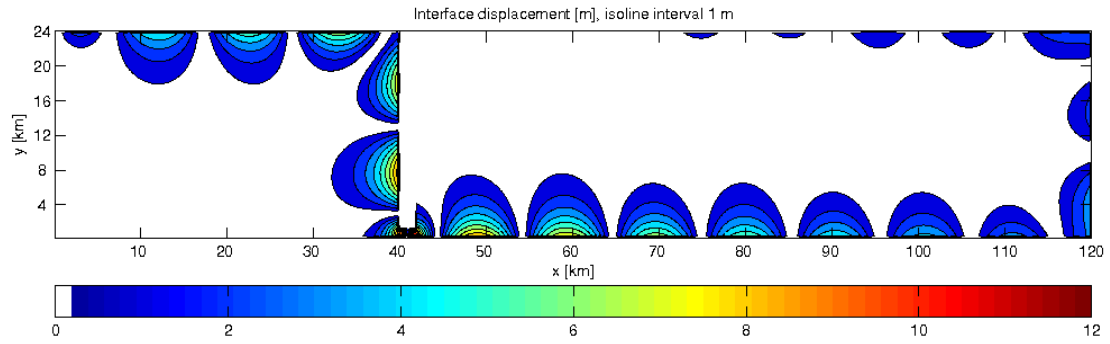

Figure 5.5: *Contour plot similar to figure 5.4, but with friction included.*

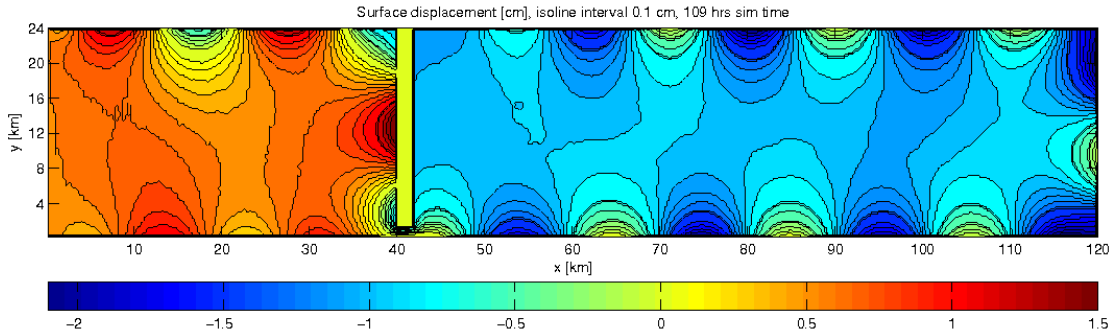

Figure 5.6: *Surface amplitudes of the run with friction, after 109 hrs simulation time. 0.1 cm isolines. Note the slight difference in mean amplitude outside and inside the constriction point.*

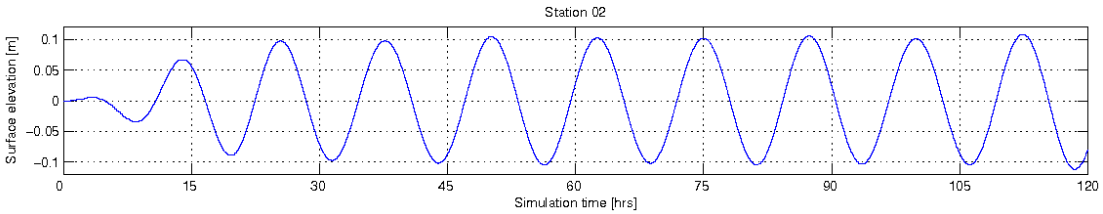

Figure 5.7: *Time series of surface amplitude at station 02, see figure 5.3.*

5.2.2 Modelling the drift

We have now established an internal Kelvin wave. In this section we want to model the drift pattern resulting from the wave motion. In order to do this properly, let us redesign the simulation area somewhat. The simulation area is now the area enclosed by the walls B,C,D, and the open boundary A'; see figure 5.8. The wave propagating along wall A is accordingly outside this model domain. The boundary A' is situated a distance from the wall corresponding to the internal Rossby radius of this wave. The forcing in this model run is thus the excess drift term $\bar{V}$ of this wave, as given in the expression (4.3.17), taken at $y = a$. Figure 4.1 shows the similar scenario in a semi-infinite ocean. The outward drift in that figure is the forcing we want to apply here.

In this model run we utilize the reduced gravity mode of the model (see Appendix B). Motion in the lower layer is thus neglected. The forcing in this model run is the mean drift, currents that do not vary in time. We seek an understanding of how the mean flow develop in the upper layer of the basin.

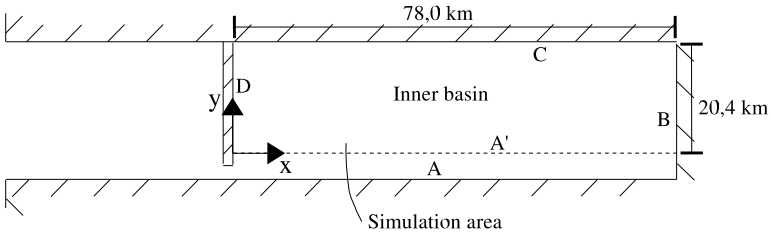

Figure 5.8: *Sketch of the drift model domain. The surrounding geometry is included to show similarities with figure 5.3. Note the displaced axis system, indicating one corner in the simulation area.*

Setup 1

Based on results from section 5.2.1, we take $\hat{\xi} = 10$ m. The maximum value for $\bar{V}$ is found from equation (4.3.17) accordingly:

$$\bar{V}_{max} = \frac{c_1}{2H_1}\hat{\xi}^2\left(1 - e^{-2}\right)\frac{K}{2f} = 0.043\,\mathrm{m}^2/\mathrm{s}. \tag{5.2.1}$$

The boundary condition along wall A' is an inflow on the form $\bar{V}_{max}e^{-2\alpha x}$, where α is calculated in table 5.2. A problem now is to apply such a boundary condition and at the same time satisfy the continuity equation. In the first run we neglect this problem by applying the drift as an inflow across the entire open boundary. There will be a net accumulation of mass in the basin, and the mean interface will move downward accordingly. This is not physical, however the resulting quasi-stationary flow pattern may still be of interest.

The results are presented in figures 5.9 to 5.12. The first is a streamline plot, and second is a contour plot of current magnitudes. Figures 5.11 and 5.12 are contour plot of the u and v-currents respectively. The snap shot is taken after 180 hours simulation time, when the system has established the quasi-stationary state. We see a clear cyclonic behaviour from the streamline plot, with a convergence centre in the left part of the basin. There are local maxima in amplitudes near the walls at all four sides, and the maxima seems shifted toward wall B. The largest value of 0.6 cm/s is on wall A'. The amplitudes aproach zero at the convergence centre.

Setup 2

We now modify the previous setup to prevent the mass accumulation in the basin. We assume that no flow is allowed to penetrate toward the lower layer. According to results from the previous model run, we should then allow some

outflow at the southwestern corner of our simulation domain. Let us then say that from some point x_{min} the boundary condition is as formulated in setup 1. For $x < x_{min}$ the flow is following some unknown pattern, however two conditions must apply:

1. $\bar{V}$ must be continous in $x = x_{min}$
2. The integral of $\bar{V}$ across the entire boundary must be zero.

Let us use the internal Rossby radius as a measure of the horizontal scale of outflow. Allowing for some mixing zone we then set $x_{min} = 2a$, assuming undisturbed inflow for $x > 2a$. Concerning the shape of the outflow, let us for simplicity assume a linear profile on the form

$$\bar{V} = C_1 x + C_2 \qquad x < x_{min}. \tag{5.2.2}$$

Using the conditions above along with $\bar{V}|_{x>x_{min}} = \bar{V}_{max} e^{-\alpha x}$, the constants become

$$C_1 = \frac{2\bar{V}_{max}}{x_{min}} \left[1 - \frac{1}{\alpha x_{min}} \left(e^{-\alpha x_{max}} - e^{-\alpha x_{min}} \right) \right] \tag{5.2.3}$$

$$C_2 = \bar{V}_{max} - C_1 x_{min}, \tag{5.2.4}$$

where $x_{max} = 78$ km is the coordinate of wall B. Inserting values from tables 5.1 and 5.2, the maximum calculated outward current value is 2.2 cm/s.

The results after 180 hours simulation time are presented in figures 5.13 to 5.16, along with a plot of the interface height in figure 5.17. The streamlines close to wall B now follow the wall as in the previous setup, however in the rest of the simulation area the streamlines turn left immediately, gathering at wall D and propagate toward the forced outflow region. The current magnitudes decrease toward the right, approaching zero in corner B/C. A saddle point is shown in the upper left part of the basin, with somewhat larger amplitudes closer to wall C. Across wall D, the current gradient is steep, with a dominant current maxima of 3.7 cm/s in corner D/A'. The interface is negative along wall B and in corner B/C. Closer to the outflow region the layer gets successively thinner, with a maximum value of the interface displacement of 1.03 m.

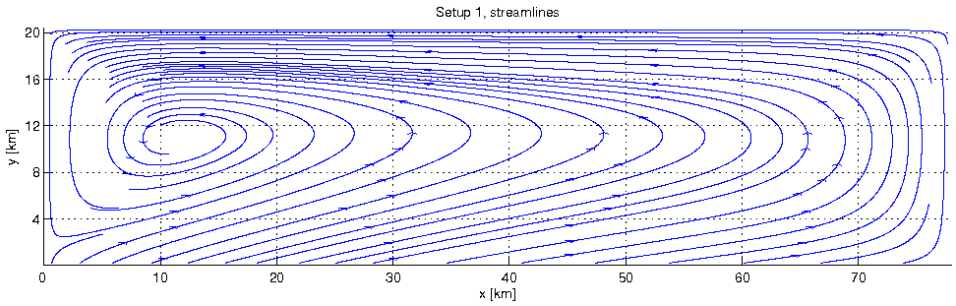

Figure 5.9: *Streamlines for drift run setup 1 after 180 hrs simulation time. Geometry as shown in figure 5.8. Lower boundary is open, and the other boundaries are closed.*

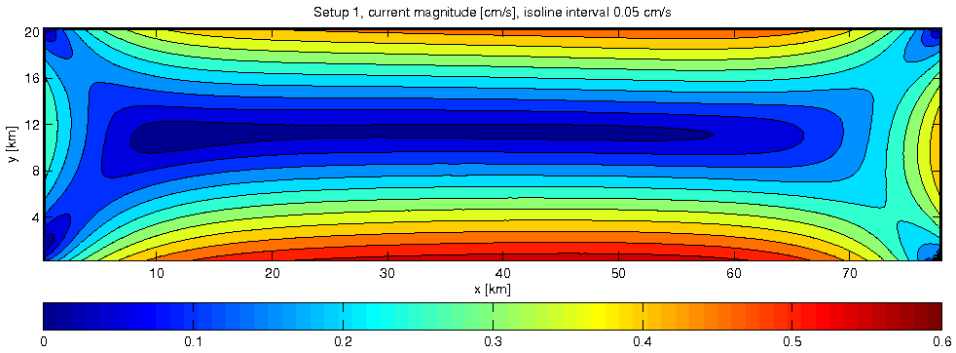

Figure 5.10: *Current magnitudes corresponding to the streamlines in figure 5.9. Isoline interval is 0.05 cm/s.*

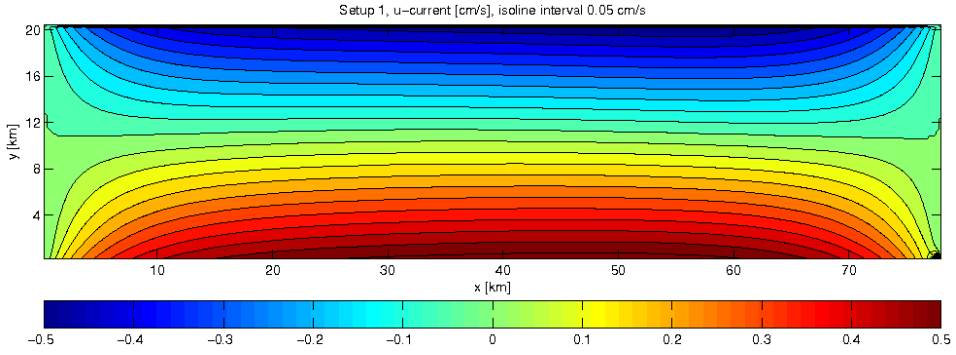

Figure 5.11: *U-current for drift run setup 1, corresponding to the streamlines in figure 5.9. 0.05 cm/s isolines.*

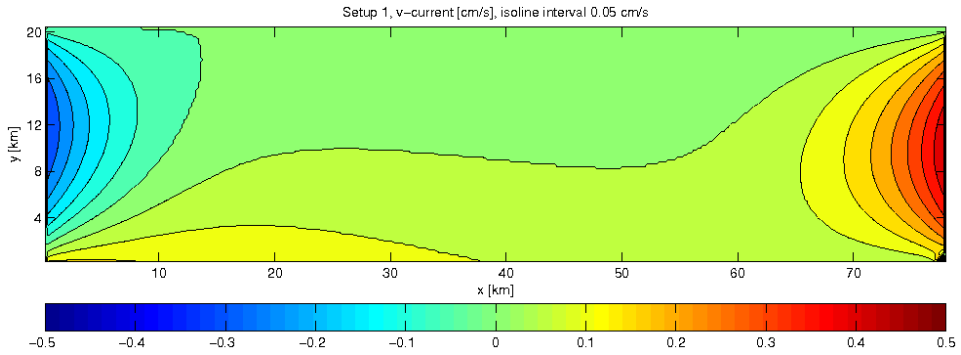

Figure 5.12: *V-current for drift run setup 1, corresponding to the streamlines in figure 5.9. 0.05 cm/s isolines.*

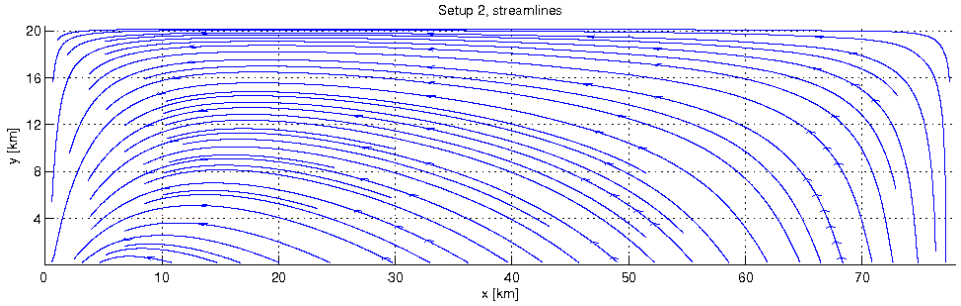

Figure 5.13: *Streamlines for drift run setup 2, after 180 hrs simulation time. Geometry similar to that of figure 5.9.*

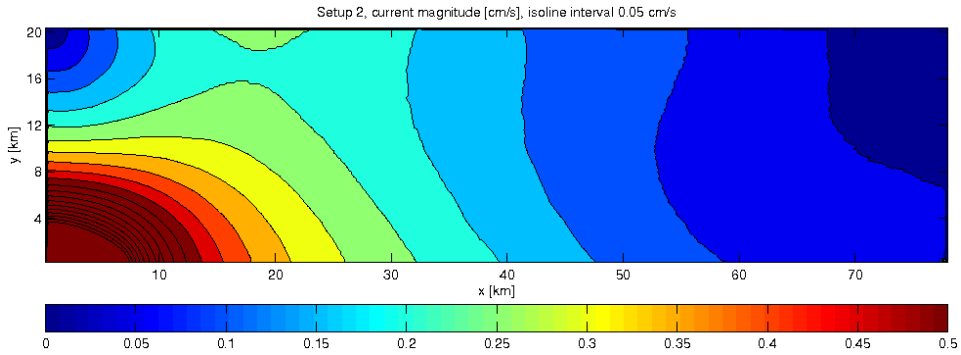

Figure 5.14: *Current velocities for drift run setup 2, corresponding to the streamlines in figure 5.13. 0.05 cm/s isolines. In the lower left corner, the velocities surpass the 0.5 cm/s treshold.*

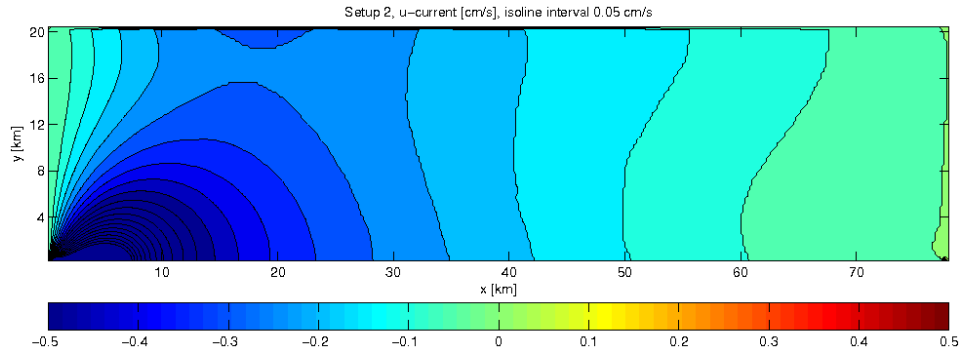

Figure 5.15: *U-current for drift run setup 2, corresponding to the streamlines in figure 5.13. 0.05 cm/s isolines.*

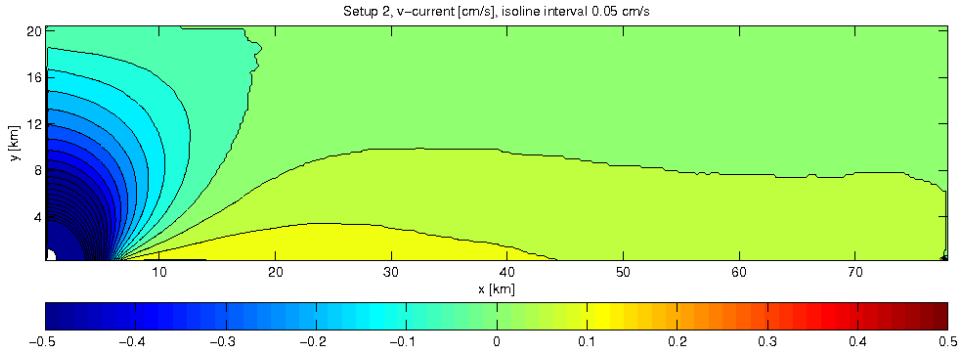

Figure 5.16: *V-current for drift run setup 2, corresponding to the streamlines in figure 5.13. 0.05 cm/s isolines.*

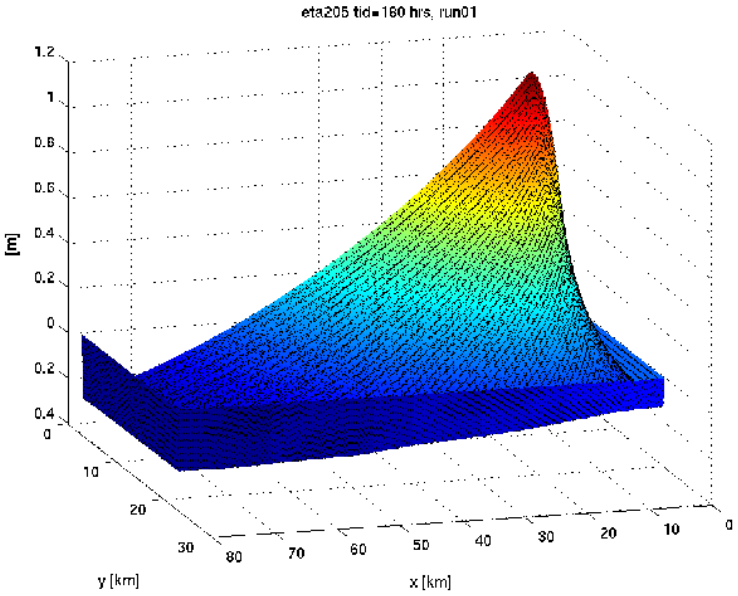

Figure 5.17: *Interface amplitude for drift run setup 2 after 180 hrs simulation time. The upper right corner on this figure corresponds to the lower left corner of figure 5.13.*

5.3 Summary and interpretations

This chapter starts by describing a theoretical basin on the northern hemisphere. A two-layer fluid is assumed, under influence of constant-frequency barotropic forcing through a small entrance. It is argued in favour of the development of an internal Kelvin wave propagating around the basin with the coast on its right. The amplitudes of these waves are supposedly much larger than the forcing amplitudes. The wave drift arguably give rise to a circulation in the basin, both when neglecting friction and when including it.

The first order model run

In section 5.2 a numerical model is applied as an attempt to verify this motion. As the plots show, there is indeed a large-amplitude internal Kelvin wave present. The wave propagate around the basin with the wall on its right, almost without changing its shape. Including friction, the amplitudes are decreasing smoothly as expected. In fact, for the forcing amplitude of

about 5 cm, the resulting internal wave amplitudes are strikingly large, and whether the waves in reality truly reach such amplitudes is indeed questionable. This will be discussed further below.

We conclude that the described forcing and geometry will give rise to an internal Kelvin wave of large amplitude in the basin. The amplitude of the wave is dependent on the forcing, and the shape of the basin entrance. From these model runs it is not possible to extract precise quantitive information, only suggestions of order of magnitude.

Regarding the results for the surface, there is not much to point out. The 12.4 hour oscillations in the mean surface level are evident, and the amplitudes are of the same order as the forcing. There are also traces of a smaller wave component, being the surface projection of the internal Kelvin wave.

The drift run

In order to simulate the drift in the waves properly, a full nonlinear model is needed. Such advanced modelling is however beyond the scope of this thesis. Our approach is utilizing a more experimental setup, which still have showed some interesting results.

The main problem is to formulate a proper boundary condition. We have no information regarding the interaction between the return wave propagating along wall D, and the initial wave propagating along wall A. Even more problematic is the case when the wave is damped down before reaching around the basin. In reality, there is a possibility that water in the upper layer is propagating down in the water column and travelling back toward the entrance in the lower layer. This process is neglected in the model. Two different setups are applied, in order to single out different properties of the solutions.

The intention of setup 1 is to show how the Coriolis force affects the drift, by creating a cyclonic circulation. The accumulation of mass is unavoidable, but as the results show, the cyclonic behaviour is a dominant feature as predicted.

With the results from setup 1 in mind, we create setup 2. The problem with this setup is that outflow is forced at the same time as the drift inflow forcing occur. In reality, there would first be inflow from the wave, then accumulation of mass leading to pressure gradients forcing the water out along wall D. However, after a long simulation time the same equilibrium state must be reached in either case. Looking at the results, we see the lowering of the interface in the upper right part of the basin as conjectured previously.

The streamlines follow the isobars around this corner, with the flow in geostrophic balance. The mentioned saddle point in the upper left part of the basin, is a result of streamlines closing together. As they approach wall D, they rapidly turn downward and experience a relatively large acceleration in the flow. This is indicated by the isolines in the contour plot.

The conclusion from this section is as follows: Due to a decay in alongshore wave averaged drift, excess flow is propagating towards the interior of the basin. This flow is affected by the Coriolis force and is deflected to the right, and mass accumulation occurs in the upper right part of the basin. Basin geometry, frictional damping and other factors influence this motion. Due to mass accumulation, the interface is forced downward. The resulting pressure gradient forces the flow outward and toward the right. After a steady state is reached, the flow is streaming along the isobars. The streamlines gather in the left part of the basin where the flow abruptly turns downward and accelerates toward the exit.

Limitations of the model regarding the first order run

This model does not include effects regarding vertical mixing. There are no tests comparing wave amplitudes to upper layer thickness. As such it is difficult to resolve the process around the basin entrance properly. Accordingly we must take care when interpreting quantitive properties of the solution. It should be kept in mind that the barotropic forcing have amplitudes of order 5 cm, and the resulting waves in the inner basin have amplitudes of order 10 m. If we apply a forcing which is ten times larger, the internal waves in the interior would become ten times larger as well, due to the linearity of the model. This, of course, clearly violate the implicit demand on the internal wave amplitude to be smaller than the upper-layer thickness.

Another important aspect is the flow through the vertically constricted area. With large gradients in the bottom topography, the vertical motion of the flow can not be neglected, and there will not exist a simple two-layer density distribution close to the constriction point. Furthermore, vertical mixing will give rise to turbulent Reynold stresses, damping the flow (LeBlond and Mysak, 1989). Hence, the amplitudes inside the basin should definitely be smaller than the model results.

Chapter 6

A realistic application

It is tempting to apply the present theory to a more realistic setting. In chapter 5 we looked at a semi-enclosed basin with an opening of small cross-sectional area. The internal Kelvin wave propagating around this system arguably gave rise to a circulation pattern. The question now is whether there exists some place in the nature where this result may be applied. In this chapter we will look at the Van Mijen fjord in Svalbard, to examine whether there may be a tidally driven internal Kelvin wave inducing a mean circulation pattern in this fjord.

6.1 The Van Mijen fjord

The Van Mijen fjord is an arctic fjord, situated at N 77.8°, E 15.5°. The entrance is covered by a wide island, Akseløya, limiting water exchange to two narrow sounds, Akselsundet in the north and Mariasundet to the south, see figure 6.1. Akselsundet is 1.1 km wide with a sill depth of 32 m, whereas Mariasundet is divided in two small passages, one in the north being 0.2 km wide and 2 m deep, and a 0.5 km wide and 12 m deep passage in the south (Bergh, 2004). The interior is divided in two basins, where the outermost basin is the target of our investigation. In this basin the west and southern coast are very steep down to about 80 m, and max depth in the interior is about 115 m.

The tidal motion outside the fjord is forcing water through the sounds, and during flood periods the water enters the fjord as jet currents (Bergh, 2004). During most of the wintertime the fjord is covered by an ice lid, as Akseløya prevents the ice from blowing out of the fjord. This ice is maintained long into early summer, which reduces the wind from disturbing the motion in the water.

Fresh water runoff is limited to glacial melting during summer, where a

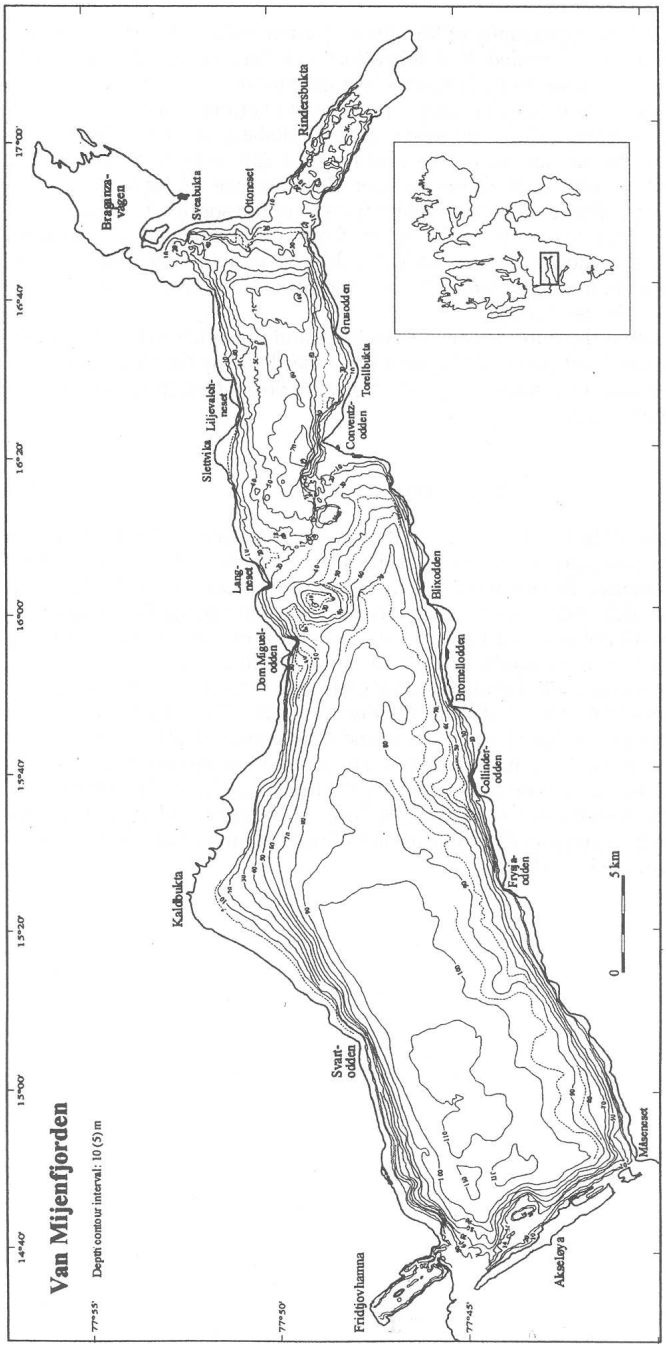

Figure 6.1: *The Van Mijen Fjord topography (Bergh, 2004).*

two-layer system develops in the water column. During winter the density gradient becomes gradually less pronounced. Density profiles are presented

in Bergh (2004) based on CTD (Current Temperature Depth) measurements performed March-April 2003. An example plot is shown in figure 6.10, from measurements 11th April. The CTD-section is indicated as the dotted line in figure 6.2. The station VM6S is showed specially. From the density profile we see a weak pycnocline at station VM6S. The density change over 40 meter is 0.1 kg/m^3. Further north the pycnocline fades.

6.2 Another model run

In chapter 5 we look at a rectangular box, and perform a model simulation of this geometry. We will now apply the same model to a bottom topography representing the Van Mijen fjord and the area outside. In this chapter, however, we restrict ourselves to model the waves in the fjord. The topography is too to complex to model the drift properly.

The main intention of performing these model runs is to verify the internal Kelvin waves in the fjord. However, some interesting topographic effects have been revealed throughout the study, namely the interaction between the Maria Sound and the Aksel Sound. Thus, we will spend some time looking into these effects as well.

6.2.1 Model setup

Bottom topography

A plot of the bottom topography is presented in figure 6.2. This bottom matrix is constructed manually by professor Bjørn Gjevik, using direct map readings. The horizontal grid distance is 200 m. The coast outside Akseløya is sampled with a grid distance of 1000 m, and later interpolated to 200 m.

Forcing and input parameters

The model is run with tidal forcing. To get approximate values for the harmonic constants, values from Longyearbyen is used. According to Norges sjøkartverk (1993), the dominant tidal component here is the M_2 component with an amplitude of 52.2 cm. We choose to use this data in the Van Mijen system. The forcing is accordingly oscillation in the surface and interface, along the western boundary. The period is 12.4 hours, and surface amplitudes are according to data from Longyearbyen. In the interface a reduced amplitude is applied.

The remaining input parameters are presented in table 6.1, equivalent to what is done in section 5.2. Based on these values we calculate properties of an internal wave, shown in table 6.2. Here we choose H_1=30 m. This

corresponds to the depth of the Aksel Sound, where most of the water mass exchange takes place (Widell, 2006). An important note is regarding the choice of the relative density difference $\Delta\rho/\rho$. The value chosen is not based on real measurements, it is rather a test of how the wave system in the fjord will respond if this stratification is present.

Parameter	K [s^{-1}]	H_1 [m]	$\Delta\rho/\rho$	g [m/s^2]	ω [s^{-1}]	f [s^{-1}]
Value	1.4e-5	30	0.001	9.81	1.41e-4	1.42e-4

Table 6.1: *Model input parameters, similar to table 5.1.*

Three run setups

Wave generation in the Van Mijen fjord takes place in two different sounds. It is chosen to perform three runs; Setup 1 keeping the original bottom topography, Setup 2 closing the the Maria Sound to the south and Setup 3 closing the Aksel Sound to the north. The closing of the sounds is done by simply editing the bottom topography matrix directly.

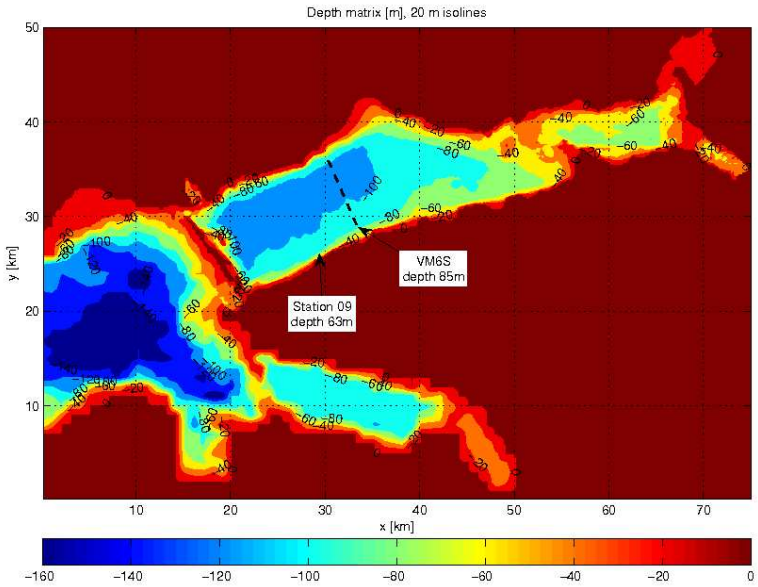

Figure 6.2: *Bottom matrix, the Van Mijen fjord and surrounding area. 20 m isolines. Station 09 and VM6S are indicated. The dashed line corresponds to the CTD-section plotted in figure 6.10.*

Parameter	Expression	Value
c_1	$\sqrt{gH_1\Delta\rho/\rho}$	0.54 m/s
a	c_1/f	3.8 km
λ	$2\pi/k = 2\pi c_1/\omega$	24 km
α	$K/2c_1$	1.3e-5 m^{-1}

Table 6.2: *Calculated parameters, similar to table 5.2.*

6.2.2 Results and comments

Setup 1

Figure 6.3 shows a contour plot for setup 1, which is the actual Van Mijen bottom topography. It is the absolute value of the interface elevation that is plotted, only amplitudes over 5 m are shown. The snapshot is taken after 119 hours simulation time. The intention of this plot is to show the presence of the internal Kelvin wave. As seen, the wave is following the wall, propagating inwards with a horizontal decay in amplitude. The maximum amplitude at the southwestern wall is up to 16 m, and the next local maximum on the southeastern wall is 10 m, followed by a maximum of 8 m. Just as the wave starts propagating back along the north wall it is damped below the 5 m treshold.

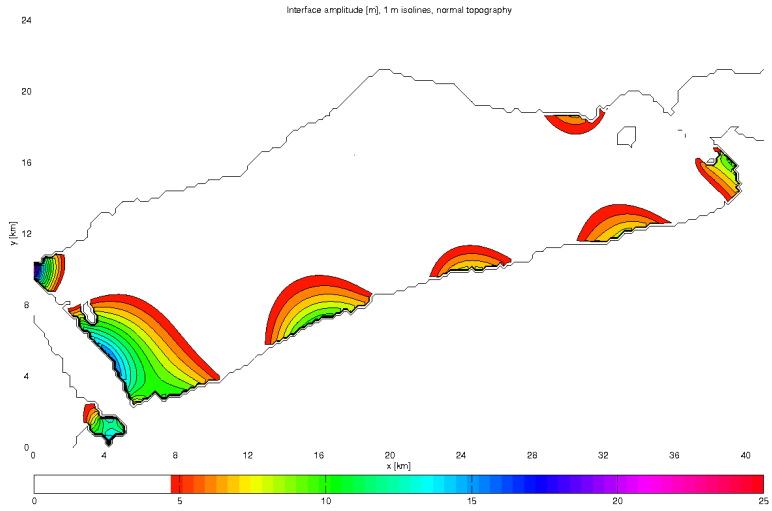

Figure 6.3: *Interface elevation after 119 hrs simulation time, original Van Mijen bottom topography (Setup 1). 1 m isolines. Only contours from 5 m and upwards are shown. The black line indicates an outline of the coast. Note that the Maria Sound is open though this is not shown in the coastline.*

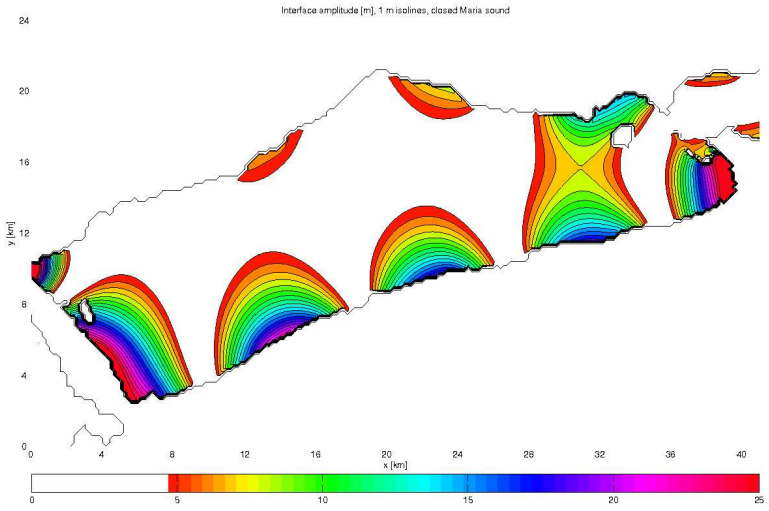

Figure 6.4: *Interface elevation similar to that shown in figure 6.3. This time with the Maria Sound to the south closed (Setup 2).*

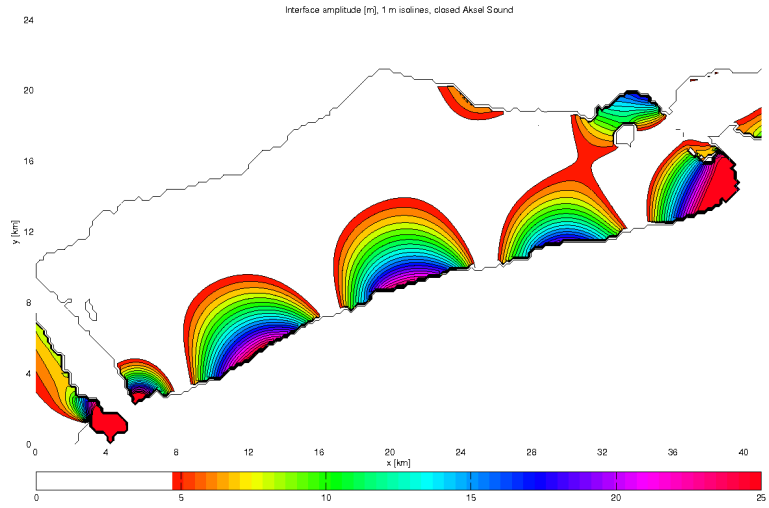

Figure 6.5: *Interface elevation similar to that shown in figure 6.3. This time with the Aksel Sound to the north closed (Setup 3). Note that the Maria Sound is open though this is not shown in the coastline.*

Setup 2 and 3

With setup 2 we close the Maria Sound to the south, and with setup 3 the Aksel Sound to the north is closed. In the same manner as in figure 6.3, contour plots of setup 2 and 3 are shown in figures 6.4 and 6.5 respectively. The amplitudes in these plots are over 26 m, much larger than in setup 1. There is still a horizontal damping of the wave; the amplitudes are reduced with a couple of meters from one maxima to the next. These two wave systems look rather similar, when not taking the different generation points into account.

A timeseries comparison plot

Figure 6.6 shows a timeseries plot comparing the three runs at station 09 (see figure 6.2). Also included is a plot showing the amplitudes from setup 2 and setup 3 added together. What we see here is that setup 3 generates the largest amplitudes, around 26.5 m. Setup 2 have amplitudes around 23,5 m, only 11% smaller. Another feature that is more striking is the difference in phase. The contour plots does not separate wave crests from throughs, but here it is evident that the two wave systems are in near opposite phase. There must accordingly be destructive interference between these two waves. This is evident in the plot where the waves are added together. The resultant wave has reduced amplitude. The wave from setup 1 has even less amplitude, however this is readily explained. When the wave propagates northward outside Akseløya, some of its energy is used to generate the wave at the Maria Sound. There is accordingly less energy available to generate a wave at the Aksel Sound, and the resulting wave amplitude here must be reduced.

The interaction between the sounds

Determining the actual wave system in the Van Mijen fjord requires more extended model runs than what is done here. It is not given that the interaction between the sounds result in destructive interference as is the case in this model setup. With different choice of upper layer thickness and relative density difference, the internal phase speed will change accordingly. The wave interaction is strongly dependent on the time it takes for the wave from the Aksel Sound to reach the Maria Sound. As the period of the wave remains constant, this is actually the only factor determining the phase difference of the two wave systems.

Comparing analytical and numerical results

Table 6.2 shows calculated properties of an internal Kelvin wave. The assumptions behind this calculation are as described in chapter 3; namely

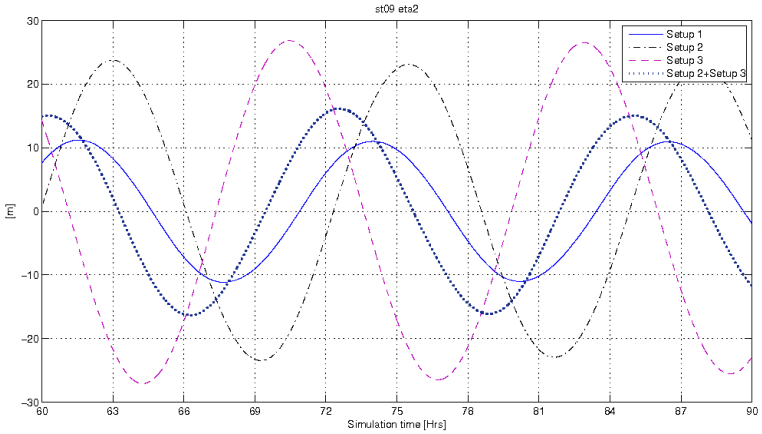

Figure 6.6: *Time series of interface elevation between 60 and 90 hrs simulation time at station 09, see figure 6.2. The solid line (Setup 1) is for normal Van Mijen topography, the dash-dotted line (Setup 2) is with Maria Sound closed and the dashed line (Setup 3) is with Aksel Sound closed. The dotted line is the calculated sum of the data from Setup 2 and Setup 3.*

semi-infinite ocean, two-layer system with infinitely deep lower layer and $|\eta| \ll |\xi|$, along the usual incompressibility relation and hydrostatic pressure distribution. In the numerical model we make the same assumption regarding incompressibility and the two-layer density profile. However this basin is not semi-infinite, neither is the lower layer infinitely deep. We should accordingly take a closer look at the tabulated values to check if they coincide with the model results.

From the plots 6.3 and 6.6 it is possible to extract approximate values by inspection. Data from setup 1 is used. The results are a=3.44 km, λ=18.2 km and T=12.5 hrs. We may then calculate the phase speed

$$c_1 = \omega/k = \lambda/T = 0.40\text{m/s}. \tag{6.2.1}$$

In order to get a reasonable estimate of α, we need measurements of a wave propagating relatively undisturbed for several wavelengths. This is needed in order to be able to measure the degree of horizontal wave damping as a result of friction. In the Van Mijen simulation area, topographic effects disturb the propagation of the Kelvin wave after about 1.5 wavelengths. The conditions are thus not in favour of making any reasonable estimates of α.

From the other estimated values there are comments to be made. Firstly, it should be kept in mind that the method of obtaining these values is direct inspection, and is subject to a relatively large margin of error. The period

is very close to the forcing period 12.4 hours, which was to be expected. The wavelength is somewhat shorter than calculated, though at the correct order of magnitude. There is surprisingly good agreement for the internal Rossby radius. The difference in phase speed is a direct consequence of the difference in wave length.

The following must be concluded: The wave system in the Van Mijen fjord, produced by the numerical model, is in fact quite close to a wave system in a semi-infinite ocean with infinitely deep lower layer, as discussed in section 3.2.

Limitations of the model

We will here repeat briefly the main points from the discussion of the model in the previous chapter. This is a simple model, the friction is linear and there is no vertical resolution. The energy loss in the sounds due to turbulent mixing is not taken into account. There is nothing in the program code to prevent the internal wave amplitude to surpass the upper layer thickness. As there are no nonlinear terms in the model equations, the drift terms derived in section 4.3.2 will not be present in the model. The resulting wave amplitudes are too large. However, the presence of an internal wave of some amplitude is evident.

6.3 The motion in the Van Mijen fjord

In the following, an attempt at describing the modelled wave-induced circulation in the Van Mijen fjord. We will look at the assumptions behind the analytical and numerical model, in order to try to understand how the model relates to the actual fjord.

6.3.1 The wave-induced circulation

Model summary

In the previous section, a numerical model is utilized to identify an internal Kelvin wave in the Van Mijen fjord. We have assumed an upper layer thickness of 30 m and a relative density difference of 0.001. With this model setup we get an internal wave with amplitudes of order 10 m. The wave system is comparable to a wave in a semi-infinite ocean with an infinitely deep lower layer, as derived in section 4.3.2. We have found that waves are generated in both the Maria Sound and the Aksel Sound, and the amplitudes from these two generation points are of comparable magnitude. The amplitude of the resultant wave is dependent on the internal phase speed of the waves.

Comparing drift results from the rectangular box

Let us then look at the wavelength and period of the resultant wave from this model run. Comparing to the previous chapter, where a rectangular box is studied, we realize that these properties are rather similar. Accordingly,

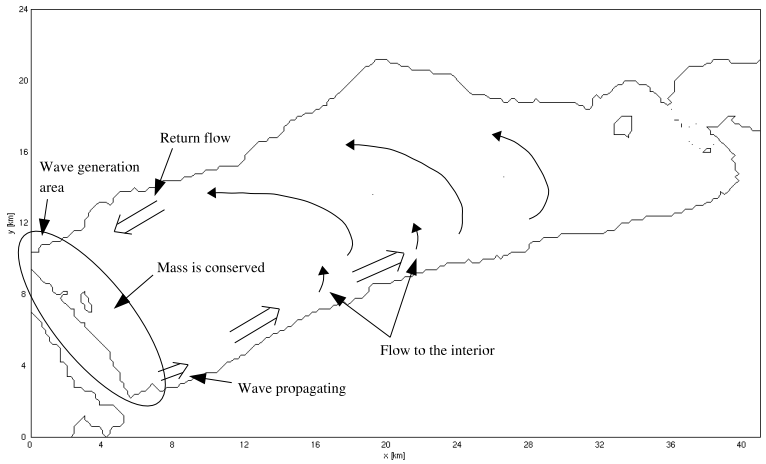

Figure 6.7: *Sketch of the circulation pattern in the Van Mijen fjord. The oval enclosing both the sounds indicates the wave generation area. Here mass is conserved, with a wave propagating inwards along the southern boundary.*

the drift pattern found previously may also apply to the Van Mijen fjord. Due to the complexity of the Van Mijen coast geometry, we do not perform a drift run here. We hypothesize the following conclusion (see figure 6.7):

As long as there is an internal Kelvin wave, there will be Stokes drift. This drift leads to transport of mass. With friction present, there will be flow into the interior of the basin due to the reduction of the Stokes drift. This excess drift must follow some pattern and end up somewhere along the northwestern part of the fjord. At the wave generation area, the mass flux following the internal wave must be compensated by equal amount of inflow from the interior due to continuity.

It will not be attempted to make estimates of the actual mass circulation due to wave drift in the Van Mijen fjord in this thesis. From equations (4.3.16) and (4.3.17) it is trivial to calculate the drift terms. However this is based on knowledge of wave amplitude and density distribution. This information must be obtained from field measurements.

6.3.2 A closer look at the assumptions

Several assumptions are made throughout both the analytical work, as well as in the numerical model. We will in the following look at the most important assumptions in turn. This will give information regarding the validity of our results in Van Mijen fjorden.

Interface amplitudes much larger than surface amplitudes?

Figure 6.8 shows a time series plot of surface and interface amplitudes at station 09. Upper layer amplitudes are of order 0.5 m, whereas interface amplitudes are greater than 10 m. We conclude that this condition is met.

Negligible motion in lower layer?

Figure 6.9 show a plot of current magnitude in upper and lower layer, station 09. The upper layer currents are about 0.15 m/s, whereas the lower layer current is 0.09-0.1 m/s. The upper layer currents are less than twice the magnitude of the lower layer currents. When looking at the motion further from the coast at a deeper station, the lower layer currents are reduced marginally. However they are still present to a large degree. The lower layer motion is accordingly not negligible, strictly speaking.

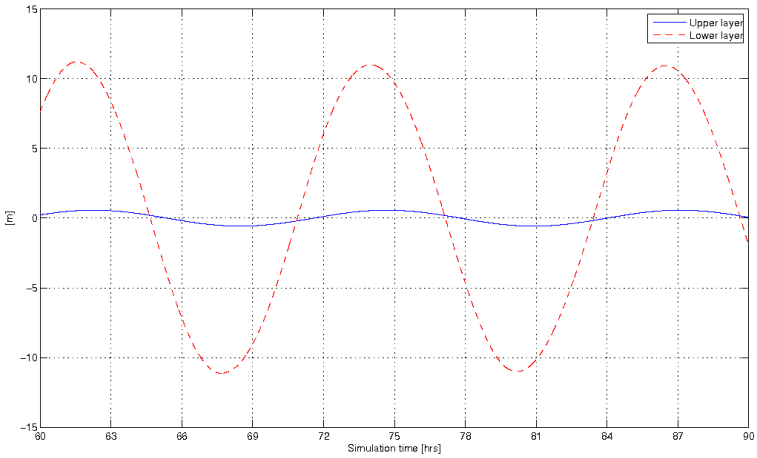

Figure 6.8: *Time series at station 09 using normal Van Mijen topography (Setup 1), between 60 and 90 hrs simulation time. The solid line shows surface elevation, and the dashed line is interface elevation.*

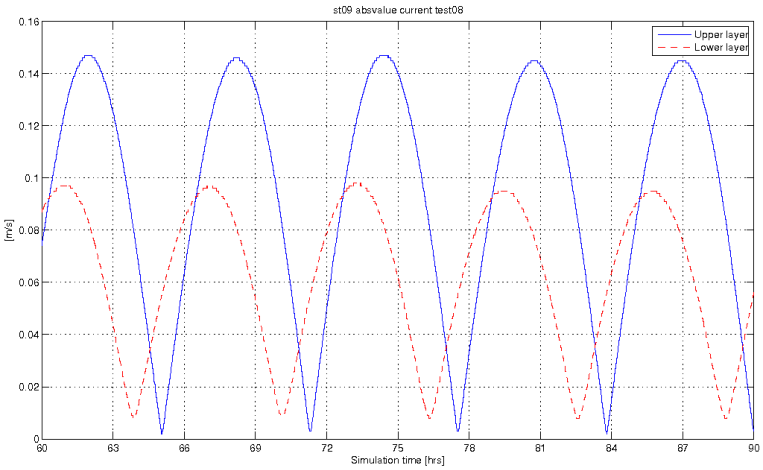

Figure 6.9: *Time series of current magnitude at station 09 between 60 and 90 hrs simulation time. Solid line is upper layer, and dashed line is lower layer.*

Infinitely deep lower layer?

The upper layer thickness is set to 30 m, whereas max depth is 115 m. The depth along the coast is 60-90 m. The lower layer is not much thicker than the upper layer. This leads to lower layer currents of non-negligible amplitudes, as found above.

Semi-infinite ocean?

Van Mijen fjorden is a large fjord. There is room for several wavelengths along the straight southeastern coast. The internal Rossby radius does not reach into the middle of the basin. The coast on the southeastern side is very steep down to about 70 m. With respect to an internal wave and after passing the Maria Sound, this geometry is very similar to a semi-infinite ocean.

Two-layer density distribution?

As described above, the stratification in the fjord is strongest during summer. When the ice freezes in autumn the two-layer system is gradually weakened. As figure 6.10 shows, there is only a marginal pycnocline in April, with a relative density difference ten times smaller than modelled. Further this stratification is only present along the southern coast.

During summer the ice melts. This gives rise to energy input from winds,

disturbing the motion in the water. Even though the stratification is intensified in this season, wind effects may dominate the internal Kelvin wave motion. It is thus difficult to determine to which degree there is a significant internal Kelvin wave in the Van Mijen fjord, and how the properties of this wave change during the year.

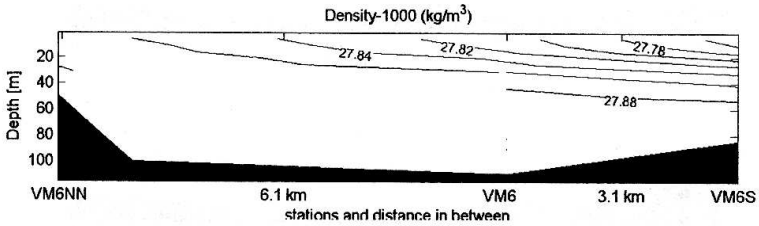

Figure 6.10: *Density profile, based on CTD-measurements 11th April 2003. The cross section is indicated in the dashed line in figure 6.2. 0.02 kg/m^3 isolines. (Bergh, 2004).*

Chapter 7

Conclusions

The main goal of this thesis is to study the drift induced by an internal Kelvin wave. This wave is then introduced into a large semi-enclosed basin. The idea is that the presence of the wave should induce a circulation in the basin. Finally, we have made an attempt at relating our theory to the circulation in the Van Mijen fjord in Svalbard.

7.1 The theory

The basic equations

The initial geometry of our problem is a two-layer system, as sketched in figure 2.1. We integrate the basic equations in the vertical, between material surfaces, to obtain equations for the drift (see Appendix A). We derive the equation set (2.2.11)-(2.2.13) governing the motion in the upper layer.

First order motion

We introduce a straight coast and apply a monochromatic wave source. The first solution of our set of equation is internal wave motion, valid to $\mathcal{O}(\epsilon)$, e.g. equations (3.2.13)-(3.2.17). Expressions for the wave energy are derived. The resulting expressions are similar to known barotropic wave energy expressions.

Second order motion

The next topic of investigation is the motion to $\mathcal{O}(\epsilon)^2$. We apply the theory of Stokes (1847), to get an expression for the drift in the internal Kelvin wave. This drift is shown to be related to the mean energy through the group velocity, in the same manner as for surface waves.

Next, we derive the second order equations from our set of basic equations.

After considering various possibilities, we have managed to derive the resulting mean flow, shown in solutions (4.3.16)-(4.3.17). One interesting feature of this flow is the $\bar{V}$-component. This component is zero if there is no friction. The alongshore component of the mean flow is shown to be similar to the Stokes drift of the first order wave, which is an expected result.

We integrate normal to the coast, to get the total mass transport in the alongshore direction from the wave. The transport is effectively confined to a distance of $2a$ from the coast.

It is shown that the right hand side of our second order equations (4.2.3)-(4.2.4) may be written as divergence of wave energy. This is connected to the radiation stress theory; see Phillips (1980).

7.2 Application to semi-enclosed geometries

The basin

The next step in our study is to apply the derived wave system to a large semi-enclosed basin. The geometry is constructed to enhance internal wave amplitudes in the basin. These waves will then propagate around the basin with the wall to its right.

A numerical model is applied to this system. The first two runs verify the existence of internal Kelvin waves in the basin. One run is without friction, and the other with linear friction, damping the wave amplitudes as the wave progress. The next runs utilize data from the run with friction. The excess flux $\bar{V}$ (see equation (4.3.17)), from the initial wave, is used as forcing, and we want to examine how the flow develop in the interior.

Without friction, there is apparently a mean circulation present. However there are problems connected to interference when the wave has reached around the entire basin. Thus we restrict ourselves to cases where the wave is not able to propagate around the entire basin. The streamlines indicate a somewhat complicated circulation pattern. The flow is affected by the Coriolis force. However, the mean interface is pushed down in the corner opposite to the wave generation area. The resulting pressure gradient leads to the development of a flow in geostrophic balance.

The Van Mijen fjord

We finally examine the possibility of finding the studied phenomenon in reality. The Van Mijen fjord is used as a test example. This fjord is covered with ice much of the year, so energy input from the wind is small. Hence,

tidally generated waves may dominate for a large part of the year.

A model run is made, assuming a relative density difference of 0.001. The result show an internal Kelvin wave of amplitudes comparable to those from the theoretical basin run. A drift run is not performed due to complexity of the fjord geometry. Nevertheless, based on the model results, conditions are in favour of a circulation pattern of some form; see figure 6.7. The real wave motion in the Van Mijen fjord is not as simple as the modeled results. Different processes disturb the two-layer system, which is the basic assumption in our work. Further investigation is needed in this particular fjord, in order to verify or eventually reject our assumed internal Kelvin wave patterns.

As an interesting side note, a unique topographic effect is discovered in the Van Mijen fjord. Wave generation is present at two different sounds. The wave systems are of comparable magnitudes. The resulting wave system in the fjord is thus a superposition of these two systems.

7.3 Future work

From this work it is clear that several problems need further investigation. In the following some ideas for future work are listed.

Theory

- Introduce Lagrangian coordinates and solve the equation of motion for a two-layer system without integrating in the vertical.
- Use a different friction parametrization, and include the specific effect of friction against ice.

Model

- Include nonlinear terms in the computation scheme of Gjevik's model. Then the drift properties could be extracted directly. This is work in progress.
- Use a vertically resolved model, with better friction modelling. The exchange of water masses between the layers need better understanding. Also, a better modelling of the turbulence around the constriction point would give more realistic wave amplitudes.

The Van Mijen fjord / other applications

- Analyze more of the available field data from this fjord. Perform new field measurements; time series at summer time, closer to the south-

eastern coast. We need measurements where we believe the internal Kelvin waves are largest.

- More extended model runs in this fjord. Look at interaction between the two sounds for different choices of $\Delta\rho$.
- Investigate other potential fjords where this process may be present. The north Atlantic basin with the equatorially bound internal waves may support this circulation.
- Apply a similar study to internal equatorial Kelvin waves, and couple it to the ENSO-problem (ENSO=El Niño Southern Oscillation).

Appendix A

On Lagrangian description of motion

Fluid motion is generally studied in one of two ways. In basic geophysical fluid dynamics it is customary to utilize an *Eulerian* description of motion, where fluid properties are described at certain points in the *field* as function of time. In this frame of reference, information on the flow connected to given geometrical points is easily extracted. However, determining a certain fluid

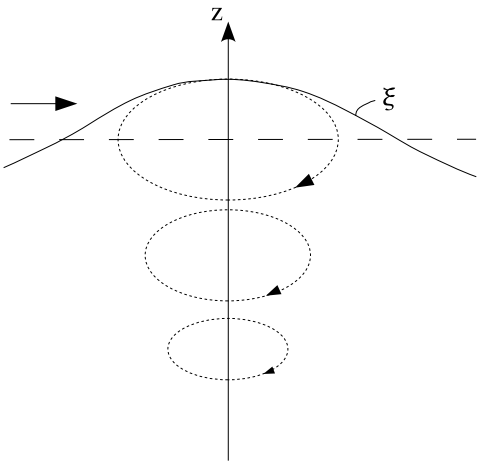

Figure A.1: *Fluid particle trajectory connected to wave motion. Wave is propagating towards the right. The particle motion is elliptic, and the motion decays to zero far from the interface.*

particle's position at a later time is far from trivial; for this a *Lagrangian* description of motion is needed. It is the Lagrangian properties of the fluid we investigate when analyzing the drift of the wave. We want to know how the actual fluid particles move in the wave motion.

It is possible to utilize Lagrangian coordinates, applying this to the equations of motion and solving the resulting system of equations. The calculations following such a procedure are however rather complex, and beyond the scope of this thesis. On the other hand the motion under investigation is that of waves in shallow water. It is thus possible to integrate in the vertical to remove some difficulties regarding vertical dependence. Care must be taken performing the integrations, to ensure that information regarding the drift is maintained. This is satisfied by choosing material surfaces as limits of integration, rather than some specific height (Broström et al., 2008).

The lowest order trajectory of a fluid particle beneath a wave is that of an ellipse, as illustrated in figure A.1. The size of the ellipse is largest at the height of the wave, and decreasing towards zero at the lower boundary. We see that the interface ξ is at the highest z-coordinate when particle motion is forward. When the particles return, ξ takes its lowest z-value. It must thus be more volume transport forward than which returns, and this is the wave drift that this thesis is all about. If the integration limits were fixed heights, the difference in volume transport would not appear, and information on the wave drift would be lost.

Appendix B

Description of the model

The model from professor Bjørn Gjevik is an incompressible hydrostatic two-layer model. For every time step boundary values are computed, and from this the horizontal volume fluxes in both layers are calculated in the interior. From this the surface and interface elevations e_1 and e_2 are calculated in the interior using the vertically integrated continuity equations in both layers directly. A forward-backward scheme is used on a c-grid, as described in Hjelmervik et al. (2005). i and j are counters along the x and y axis, such that $i, j = 1, 1$ represents the bottomleft corner in the matrix. Equations (B.1) and (B.2) shows an outline of the numerical scheme for the upper and lower layer respectively. The superscripts are just for reference, as calculations accounting for the use of a c-grid are omitted.

$$u_1^{i,j} = u_1^{i,j} - g\, c_1 h_1^{i,j} \left(e_1^{i,j} - e_1^{i-1,j}\right) + f\Delta t\, v_1^{i,j} - \Delta t K u_1^{i,j} \tag{B.1}$$

$$u_2^{i,j} = u_2^{i,j} - g\, c_1 h_2^{i,j} \left(e_1^{i,j} - e_1^{i-1,j}\right) + f\Delta t\, v_2^{i,j} - \Delta t K u_2^{i,j} - \epsilon\, g\, c_1\, h_2^{i,j} \left(e_2^{i,j} - e_2^{i-1,j}\right) \tag{B.2}$$

Here $c_1 = \Delta t/\Delta x$ and $\epsilon = (\rho_2 - \rho_1)/\rho_2$. Δx is the grid distance, and Δt is time step, determined from the CFL-criterium. K is a Rayleigh friction coefficient given as input, $h_{1,2}$ is layer depth for each layer, g is gravity and f the Coriolis parameter. u and v are vertically integrated fluxes along i-axis and j-axis respectively.

It is possible to run this model in one of three modes. (i) Either as a one-layer barotropic model solving for currents and surface elevation, (ii) a two-layer model solving for currents and elevations in both layers, or (iii) a reduced gravity mode solving for upper layer currents and interface elevation, neglecting motion in lower layer, i.e. letting the lower layer thickness approach infinity.

At the open boundaries one may specify the forcing either as current fluxes or elevation in surface and interface. The program is specially designed for boundary conditions with tidal forcing.

The program is compatible with any rectangular depth matrix, where zero depth is interpreted as land. It does not however take variation in the Coriolis parameter f into account, and should as such not be used for large-scale simulations, where β-effects may be of importance.

Output from the model are time series of currents and elevations from up to 20 stations, depth matrix of upper and lower layer, and currents and elevations of the entire area sampled at some interval. The coordinates of the stations, sampling interval of time series and field data are given as input.

Bibliography

Bergh, Jon (2004) *Measured and modelled tidally driven mean circulation under ice cover in Van Mijenfjorden*. Master thesis, Göteborg University.

Broström, Göran; Christensen, Kai Håkon and Weber, Jan Erik H. (2008) *A Quasi-Eularian, Quasi-Lagrangian View of Surface-Wave-Induced Flow in the Ocean*. Journal of physical oceanography, Vol. 38: p. 1122–1130.

Hjelmervik, Karina; Ommundsen, Atle and Gjevik, Bjørn (2005) *Implementation of non-linear advection terms in a high resolution tidal model*. Preprint Series, Department of Mathematics, University of Oslo. ISSN 0809-4403.

LeBlond, Paul H. and Mysak, Lawrence A. (1989) *Waves in the Ocean* (Elsevier Science Publishers B.V.).

Longuet-Higgins, M. S. (1953) *Mass transport in water waves*. Philos. Trans. Roy. Soc. London, Vol. 245A(903): p. 535–581.

Martinsen, Eivind A. and Weber, Jan Erik (1981) *Frictional influence on internal Kelvin waves*. Tellus, (33): p. 402–410.

Norges sjøkartverk (1993) *Tide tables for the Norwegian coast and Svalbard*.

Phillips, Owen M. (1980) *The dynamics of the upper ocean* (Cambridge university press).

Stokes, G. G. (1847) *On the theory of oscillatory waves*. Trans. Camb. Phil. Soc.

Widell, Karolina (2006) *Ice-ocean interaction and the under-ice boundary layer in an Arctic fjord*. Ph.D.thesis, University of Bergen.